Experimental examination of new separated turbulent flow validation test geometry

E. Sage Sarwas

A thesis
submitted in partial fulfillment of the
requirements for the degree of

Master Of Science In Aeronautics & Astronautics

University of Washington

2019

Reading Committee:

Owen J. H. Williams, Chair

Antonino Ferrante

Program Authorized to Offer Degree:
Aeronautics & Astronautics

University of Washington

Abstract

Experimental examination of new separated turbulent flow validation test geometry

E. Sage Sarwas

Chair of the Supervisory Committee:
Research Assistant Professor Owen J. H. Williams
Aeronautics & Astronautics

Computational fluid dynamics (CFD) is a powerful tool for aeronautic design, however current simulations are challenged by turbulent separated flows due to their complexity. A new series of experiments are required to provide insights into the simulation challenges of this flow and to assist with the validation of future turbulence models. In this thesis, initial qualification experiments are conducted for a newly proposed separated flow geometry. This validation test used an elongated hill, "speed-bump", shaped model, which was chosen because it allowed for the largest feasible Reynolds number, is longer in the spanwise direction making it more applicable to wing-like applications, is tapered at the sides to minimize side wall effects, and allows for adjustment of the flow separation via multiple parameters (i.e. incoming boundary layer, bump height, and splitter plate position). Tests were conducted over a range of Reynolds numbers, $58,000 \leq Re_h \leq 301,000$, where h is the height of the bump. Wind tunnel qualification showed high uniformity and less than 0.2% freestream turbulence, ensuring the flow was suitable for the remainder of the study. The upstream boundary layer was examined to ensure a clean inflow onto the bump. Multiple tripping devices were tested and a strip of 240-grit sandpaper was chosen for future tests. Once the trip was chosen, the experimental momentum thickness Reynolds number was used to determine the corresponding simulation inflow length, which was set to $1.5L$. China clay flow visualization and surface pressure measurements were used to examine the separated region. China clay revealed the

presence of surface vortices surrounding a strongly separated three-dimensional flow. Static surface pressure measurements also indicate slight three-dimensionality at the centerline as well as insensitivity of the separation region at higher Reynolds number. However, at lower Reynolds numbers, separation appeared to be greatly reduced. A comparison of experimental and 2D RANS simulation data showed the magnitude of the simulated pressures were similar to the experimental data, however they exhibited an opposite Reynolds number trend in the separated and recovery regions. This suggests the proposed validation geometry is a suitable challenge for current RANS models of turbulent separated flows.

TABLE OF CONTENTS

LIST OF FIGURES

LIST OF TABLES

NOMENCLATURE

a: Overheat of hot-wire

C_p: Coefficient of pressure

d: Pitot probe diameter

d^+: Non-dimensional pitot diameter $= dU_\tau/\nu$

E_w: Voltage across the hot-wire probe

h: Height of bump model

H: Vertical splitter plate location

L: Width of 3' x 3' test section

L_b: Width of bump model

R_0: Resistance at ambient temperature

R_w: Hot-wire resistance at operating temperature

Re_θ: Reynolds number based on momentum thickness $= U_\infty x/\nu$

Re_τ: Friction Reynolds number $= U_\tau \delta/\nu$

Re_x: Reynolds number based on streamwise distance $= U_\infty x/\nu$

T_0: Ambient temperature

T_w: Temperature of the hot-wire

u: Streamwise velocity component

U: mean streamwise velocity component

U_∞: Freestream velocity

u_{rms}: Root-mean-square velocity fluctuations

U_τ: Shear velocity = $\sqrt{\tau/\rho}$

ΔU^+: Boundary layer wake size

x_0: parameter controlling streamwise extent of bump geometry

z_0: parameter controlling spanwise extent of bump geometry

h_0: parameter controlling bump height

δ: Boundary layer thickness determined by where U = .99U_∞

δ^+: Displacement thickness

μ: Fluid dynamic viscosity

ν: Fluid kinematic viscosity

ρ: Density of fluid

θ: Momentum thickness

ACKNOWLEDGMENTS

There are numerous people to whom I own my deepest gratitude. To Dr. Owen Williams, for his guidance and support throughout this masters thesis project. To my parents for their love and support, regardless of my pursuits in life. To my extended family for their pride and excitement, even when I did not share it, in my work. To Dave Theno for his mentorship and friendship for over a decade. To Val Roberts and all of MESA for helping me build a solid foundation and community to stand and lean upon. To Dave Tanner and the McConnell Foundation for their moral and financial support throughout my higher education. To Dr. Jocelyn Bale-Glickman for sparking my pursuit of a formal study of fluid dynamics. To Charlie, Khai, Aron, Matthew, Anya, Vincent, Sara, Amanda, Ellie, Niamh, and Izzy for all their dear friendship over the quickly increasing years.

And to my dear partner, Chaun. Coming home to you (and our cat) is the highlight of my day. Without your love, support, and belief in me this thesis would not exist. Thank you.

DEDICATION

This thesis is dedicated to those who feel they do not belong in academia due to who they are or where they come from. We do belong and the academy is far better for having us here. May our presence open the doors for others to further reshape the academy into an accepting and supportive institution of our whole selves.

Chapter 1
INTRODUCTION

Over the past four decades the ability of computational fluid dynamics (CFD) has continued to grow due to advancements in computational power and solvers. As a result, CFD has become integral to the aerodynamic design process. However, even with these great advancements, there are still limitations in the ability of simulation models to calculate with high fidelity flows with turbulent separation. Direct numerical simulations (DNS) and large-eddy simulations (LES) are prohibitive for most engineering applications due to high Reynolds numbers. Because DNS and LES are not yet feasible due to resolution requirements, a closure model such as Reynolds-averaged Naiver-Stokes (RANS) is often used instead. While RANS works well to simulate attached turbulent flows, RANS models struggle modeling separated turbulent flows due to complexity of the flow physics. In 2014, NASA published "CFD Vision 2030" [6] and called for new modeling approaches as well as identified the need for high-quality experiments with which to validate separated flow advancements. The work outlined in this thesis aims to begin addressing this need.

Having CFD models which could reliably simulate flows with turbulent separation would have large impacts in the design stage of aircraft. Given the high Reynolds numbers and complex geometries of vehicles, turbulent separation is common and can result in loss of lift, increased noise, or losses of control authority—all of which are undesirable. As CFD continues to be incorporated throughout the aerodynamic design and testing process, there is an increasingly pressing need to capture turbulent separation in CFD models.

For a given experimental geometry, a CFD validation test case should have the following qualities: a concisely defined geometry for ease of consistency between simulation methods

and grids, be of sufficient complexity to provide a challenge for current methods, and also the ability to parametrically vary the extent of flow separation. It is also important to know the length scales of the flow to high accuracy, have closely controlled boundary conditions and to minimize any additional flow influences (e.g. side wall effects) which would be difficult to account for with simulations. When completed, this study aims to be of the highest quality CFD validation test, as classified by Oberkampf [7].

A hill-type or speed-bump geometry would satisfy the above criteria. There have previously been a limited number of studies examining the separation of flows over such geometries [8–11]. While valuable, these studies examined geometries that might have suffered from interactions with wind tunnel side wall boundary layers. It has been proposed that a three-dimensional geometry be used to avoid interactions with side walls, as this interaction would be complex and difficult to characterize. In addition, a comprehensive understanding of the flow quality (e.g. wind tunnel qualification, flow confinement) is needed for a more in-depth comparison of validation experiments and simulations.

This thesis is part of a broader project, funded by Boeing Commercial Aircraft, to conduct a series of highly-detailed and well-characterized experiments to produce a challenging and thorough CFD validation test case for turbulent separated flows. This work aims to contribute greatly to one of the broader Grand Challenge goals of the NASA CFD 2030 technical roadmap [6]. A three-dimensional speed-bump geometry is chosen, which tapers toward the tunnel side-walls to minimize side wall interference. This thesis aims to carefully control and characterize boundary conditions, examine the broad separation characteristics of geometry to ensure flow separates as desired, and to demonstrate the proposed validation test case geometry provides a challenging test of current simulation capabilities. Great care was taken in the design and execution of these experiments to ensure a concise CFD validation test domain could be defined. This includes high precision in manufacturing the bump model, qualification of the wind tunnel and splitter plate used, and careful measurements of inflow parameters.

The results of this thesis show approximate Reynolds number invariance of the separation

bubble downstream of the test geometry at high velocities. The bump geometry provides a stringent test of current simulation capabilities as initial 2D RANS simulations indicate opposite Reynolds number trends and no high Reynolds number invariance of surface pressure profiles. Overall, qualification and initial results indicate that the chosen bump geometry definition and experimental setup are suitable for further CFD turbulent separated flow validation and close examination of turbulent flow structure and the reasons many turbulence models struggle to simulate separated flows.

Chapter 2

BACKGROUND AND THEORY

New, more accurate CFD validation tests are needed for continued advancements in CFD capability. The six key aspects of a validation test identified and ranked from zero to three depending on the level of detail provided for DNS inputs by Oberkampf [7]. The six areas are: Experimental Facility, Analog Instrumentation and Signal Processing, Boundary and Initial Conditions, Fluid and Material Properties, Test Conditions, and Measurement of System Responses. The overall project, of which this thesis is a part, aims to meet the highest level of all six areas. One aspect necessary to reach this stringent criteria is that all the initial and boundary conditions of the experiment must be accurately known in order to be incorporated into simulations. Such initial and boundary condition parameters include confinement of the flow, geometry of the model and test section, relevant length scales, and knowledge of the flow quality. Detailed qualification of the equipment, facility being used, and precise measurement of flow parameters are the beginning of meeting the requirements for this validation test.

Examining the separated flow over a backward-facing step (BFS) can be informative when wanting to study other separated flows, even though the separation point is fixed for a BFS. The flow over a BFS has been continuously studied for decades due to its simple geometry yet complex and interesting flow. Figure 2.1 shows the basic set-up for a BFS experiment. Due to a sudden increase in cross sectional area, the flow experiences separation at the step and reattachment downstream. BFS have been studied to increase understanding of separation flow physics by looking at links between key parameters, such as Reynolds number, and separation phenomena such as reattachment length [12]. CFD validation has also been done using the BFS [1, 13–15].

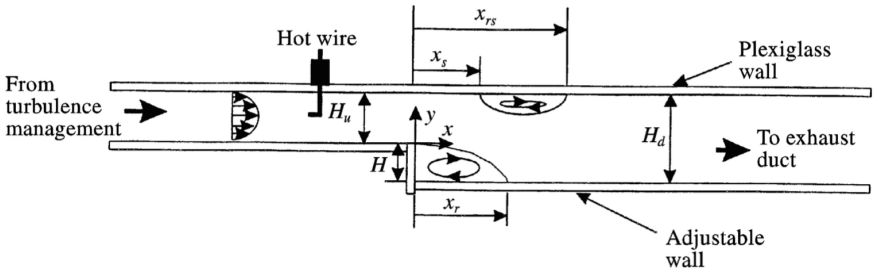

Figure 2.1: The above figure shows a basic setup for a backward-facing step experiment. The fluid flows from an inlet of height H_u into an outlet of height H_d. This sudden expansion of cross area results in a region of recirculation right at the step, height H. The flow reattaches at x_r. Figure credit [1].

While many parameters can affect the flow of a BFS, the two primary ones seem to be the Reynolds number of the flow right before the step and the expansion ratio (ER). Both the Reynolds number and the expansion ratio have more than one characteristic length. Reynolds number can be defined using the hydraulic diameter of the inlet [13, 16], the step height [14, 17], or the outlet height [1]. The expansion ratio is most often defined as $ER = H_{outlet}/H_{inlet}$. Flow over a bump or hill geometry have other potentially key parameters to consider, e.g. steepness of the geometry, momentum deficient. A key difference in the flow over a BFS and the flow wished to be examined in this study is the separation point of a BFS is always at the step. The point at which separation occurs over a curved geometry is not guaranteed.

Research has also been conducted on separated flow geometries which do not have a set separation point, as desired for this study. There have been numerous studies of turbulent separated flow over curved geometries for increasing understanding of these flows and for CFD validation. While these tests are valuable, validation requirements are becoming increasingly stringent. Studies have focused on bumps [2, 8] and axisymmetric hills [9, 18–20]. Some studies with potential side wall interactions were uncharacterized for two-dimensions. Numerous studies report tunnel qualification data [9, 18–20]. However, the incoming bound-

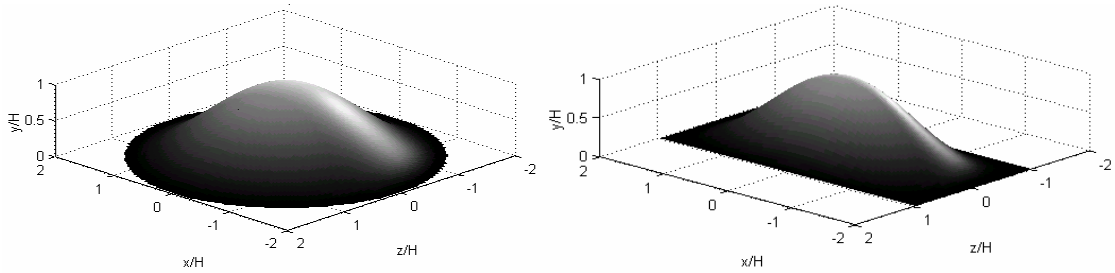

Figure 2.2: The main geometries used by Simpson and Byun are the axisymmetric hill shown on the left and the symmetric bump on the right [2].

ary layer was not always sufficiently characterized. A study of the turbulent separation over a backward facing ramp included comparisons to CFD results [21]. Comparisons between experiments and simulations were not always done in great detail [18, 21–23]. While all of the above studies have helped to increase understanding of turbulent separated flows (and in some cases CFD validation), of particular note is the work done by Simpson and Byun [2, 18, 20, 22, 24, 25], due to its extensive investigation of an axisymmetric geometry used by many to validate CFD [23, 26–29].

Simpson and Byun's [2, 18, 20, 22, 24, 25] work focused on characterizing the turbulent, often separated, three-dimensional flow over axisymmetrical and symmetrical bumps, see Figure 2.2. Their bumps were based on modified Bessel functions, and most tests were done at Re_θ = 7300. Collaborators conducted CFD simulations for comparison to the axisymmetric bump [23, 26–29]. The simulations often showed difficultly in capturing the separation see in experiments [2, 22]. Overall, Simpson and Byun's work concentrates on understanding the flow physics of turbulent separation over a bump. This deeper understanding of turbulent separated flow is very insightful to the underlying flow structure. However, studies aimed specifically at validating turbulent separated flows are still needed in order to reach NASA's goals for CFD capabilities in 2030 [6].

For this current validation test, a separated flow geometry which does not set the separation point and may be affected by a number of parameters is desired. Parameters which

may affect separation and need to be considered for any future validation test case geometry include: Reynolds number, confinement of the flow, sharpness of the bump's peak, and momentum deficit of the boundary layer. Reynolds number correlates to whether a flow is turbulent, however the affect Reynolds number has on many features in a flow tends to lessen past a critical Reynolds number. A similar Reynolds number trend is thought to happen with turbulent separation over a bump. The affect of Reynolds number on the flow over the bump geometry will be looked at in order to better understand its relation to flow separation. Most fluid experiments take place in a closed test section, such as a wind tunnel. Depending on the models vertical location in the tunnel, the confinement of the flow around the model will vary. An increase in confinement is thought to make the flow more resistant to separation on the bump. Therefore, flow confinement should be both investigated experimentally and accounted for in simulations. Since it is not desired to have a test geometry which sets the separation point (as in the case of a BFS), the bump cannot have too sharp of a peak or it will result in separation at that point. However, it must also not be too shallow or else it is very unlikely for the flow to separate. The momentum of the boundary layer is a large factor in how well a flow can resist separation. The greater the momentum near the surface, the longer it can overcome an adverse pressure gradient and resist separating. Looking at how the flow separates over a range of momentum thickness, θ, (a measurement of momentum deficient in the boundary layer) is key to better understanding turbulent separation. Examining the above parameters' effects on the turbulent separation of a bump is a key part of conducting a validation test.

Chapter 3
METHODS AND MATERIALS

All tests were conducted in the 3' x 3' low-speed wind tunnel at the University of Washington. Wind tunnel qualification focused on examinations of flow uniformity and a quantification of freestream turbulence. Measurements of the boundary layer over the flat plate were conducted using a traverse mechanism which was designed and built for this project. Flow visualization was accomplished using china clay over the bump to see the separation region macro structure. Static pressure measurements along the streamwise centerline of the plate were acquired for both the plate only and bump cases. For the bump case, static pressures were also taken spanwise (see Figure 3.6).

3.1 3'x3' Wind Tunnel

Tests were conducted in the 3' x 3' wind tunnel at University of Washington. The 3' x 3' is an open-return tunnel with a stable velocity range of 10 to 60m/s and a 3' x 3' x 8' test section. The wind tunnel has a 200hp constant speed motor with pneumatically controlled variable pitch blades. The inlet contraction ratio is 9:1 with three screens and a honeycomb section for improving flow uniformity in the test section. See Figure 3.1 for a sketch of the wind tunnel. The wind tunnel is housed in the Aerodynamics Laboratory, which has manual temperature control via ceiling vent fans open to the building exterior. The tunnel was ran for an extended period until the ambient temperature stabilized to help maintain a steady ambient temperature during tests.

In order to measure the freestream turbulence, qualification of the tunnel was done using pitot tube and hot-wire probes. The pitot probe gave mean uniformity data while the hot-wire data were used to look at the freestream turbulence spectrum of the flow.

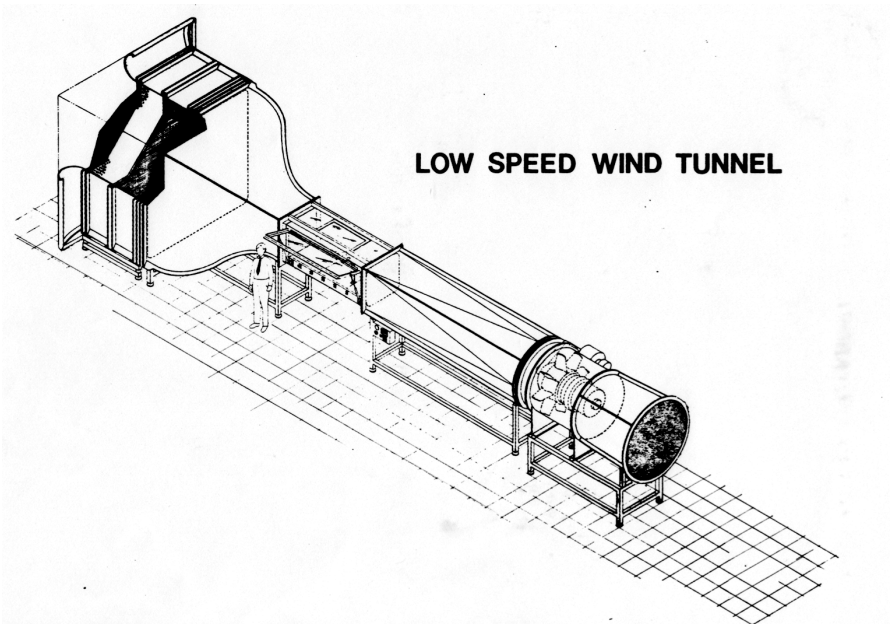

Figure 3.1: Sketch of the University of Washington 3'x3' wind tunnel. Note person next to test section drawn in for scale.

3.1.1 Full tunnel traversing mechanism for uniformity studies

In order to qualify the tunnel test section, a traversing mechanism was needed to be able to measure across the span and height of the 3' x 3' tunnel. This traverse was connected to an Arduino which controlled the vertical and horizontal position using two stepper motors and two lead screws. The traverse is able to reach nearly the entire vertical and horizontal span of the test section. Two mirrored probe holders were made to attach to the traverse sting. These probe holders extended closer to the side wall than the sting could. See Figure 3.2 of the probe holder and traverse sting in tunnel. A Baratron 226A pressure transducer, with a range of 20Torr and accuracy of 0.50%, was used for the mean uniformity data. The sting pitot tube velocity was compared to data from a stationary pitot tube farther downstream in the tunnel. This was done to account for velocity drift due to blockage as the traverse

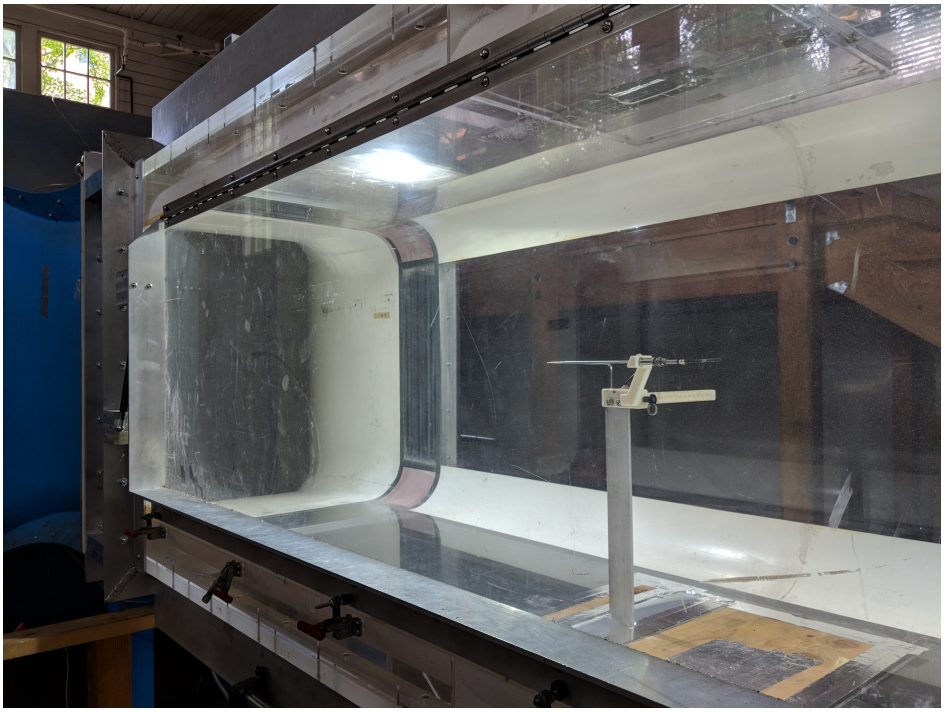

Figure 3.2: Sting traverse in test section with pitot and hot-wire probes attached on top. A 3D printed probe holder was designed for the qualification tests.

moved. The stationary pitot tube used an Omega PX653-10D5V pressure transducer with a range of 19Torr and accuracy of 0.50% of the full scale.

For horizontal uniformity, wall-offset distance was manually measured prior to each test. The flow was measured in the middle vertical position along the z-direction (i.e. left to right when facing upstream). Due to limitations of traverse travel and probe holder geometry, and in order to have an accurate wall-offset measurement, data was gathered through runs starting on both walls. These data overlapped for the approximately the middle third of the tunnel.

For the vertical uniformity, wall-offset was measured manually as well. Data was taken starting both at the top of the test section and the bottom to account for any biases in the vertical direction. The pitot tube was centered in the spanwise direction.

3.1.2 Hot-wire anemometry system

Freestream turbulence was measured using hot-wire anemometry. A 5µm wire Dantec mini probe was connected to a DISA 55M12 constant temperature bridge. The hot-wire overheat was between 0.68 and 0.8 as calculated using Equation 3.1, where R_w is the hot-wire resistance at operating temperature and R_0 is the resistance at ambient temperature, T_0. For air, an overheat value of 0.8 is desirable [30] because it is more sensitive to velocity than temperature.

$$a = \frac{R_w - R_0}{R_0} \tag{3.1}$$

The variation in overheat can be attributed to ambient changes in ambient temp for different calibrations. Using a conventional square wave test, the frequency response of this hot-wire arrangement was determined to be approximately 50kHz at the highest Reynolds number conditions (60m/s) after tuning of the internal bridge balance and high-frequency filters. The DISA hot-wire bridge output was connected to a Kronh-Hite 3384 8-pole Butterworth low-pass filter in order to remove electronic noise above the determined frequency response. The range of filter settings for the DISA bridge and Kronh-Hite filter are presented in Table 3.1. The range of filter settings values is due to multiple wires needing to be used over the course of the tests. All tests were oversampled at 200kHz. To help minimize power related noise, matched, shielded cables were used for the hot-wire probe and bridge resistances as well as an uninterruptible power supply. Power related noise was still apparent in the final results, indicating this aspect of the setup could be improved in future tests.

To minimize drift in the hot-wire calibration it was important to control the ambient temperature as much as possible. This was done by manually controlling the opening and closing of ceiling fan vents. This was particularly necessary at high velocities (e.g. 60m/s) and long test runs due to increase in ambient temperature because of the heat from the wind tunnel motor from running at high RPMs or extended period of time. Tests were not started until the tunnel had been running at full speed and for a considerable amount of time, such that the room could hit a steady state temperature as closely as possible. Using

Range of filter settings for Kronh-Hite 3384				
	Filter f	**Cut-off f**	**HW DC gain**	**HW AC gain**
Kronh-Hite 3384 filter	55.56 – 100kHz	40 – 50kHz	4.6dB	0 – 9.9dB

Table 3.1: Summary of hot-wire filter settings for the external Kron-Hite filter. Both the hot-wire DC and AC gain were applied to the output signal. The range of settings is due to multiple hot-wires being used throughout testing.

this approach ambient temperatures were controlled to within $3°C$. Further temperature correction within the calibration [31] was applied to results using Equation 3.2. In Equation 3.2, T_w is temperature of the wire, T_0 is the ambient temperature. E_w is the voltage across the wire and index r indicates value taken at the reference temperature the overheat was calculated. Before and after each test run, a calibration run was conducted at 10, 20, 30, 40, 50, and 60m/s to be used to for the temperature calibrations and corrections.

$$E_w = E_{w,r}\left[\frac{T_w - T_0}{T_w - T_{0,r}}\right] \tag{3.2}$$

3.2 Geometry for study of separated flow

3.2.1 Splitter plate

The splitter plate and bump model designed for this experiment needed to 1) have a fully developed boundary layer upstream of the bump, 2) have a three-dimensional bump, which spans the width of the test section, 3) control of the leading edge stagnation point to ensure it was above the geometric leading edge, and 4) the ability to move the splitter plate and bump to different vertical positions within the tunnel. These primary requirements informed major design decisions. Considerations of manufacturability, storability, and measurement precision also informed the overall design of the splitter plate.

Figure 3.3 depicts a CAD rendering of the splitter plate and bump within the tunnel

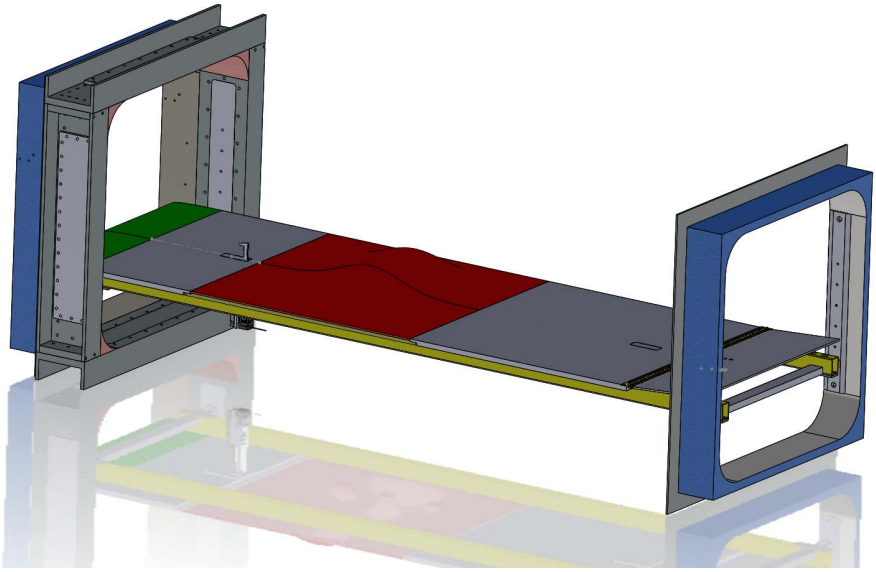

Figure 3.3: CAD rendering of wind tunnel test section with plate and bump inserted. Traverse mechanism used for boundary layer measurements is seen upstream of the bump.

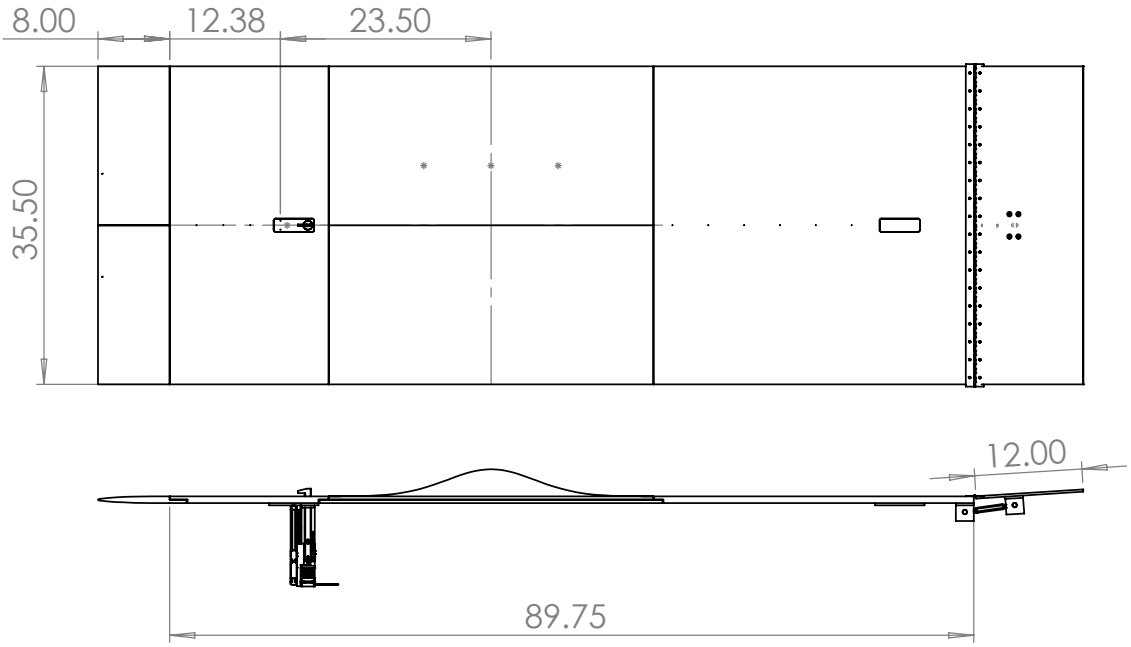

Figure 3.4: Drawing schematic of splitter plate. Units of inches. Drawing shows pitot traverse inserted in upstream position. Leading edge was 3D printed then sanded and painted in order to minimize separation of flow. Trailing edge was an adjustable flap used for setting stagnation point on the leading edge.

test section, with the walls removed. A dimensional schematic of the splitter plate is shown in Figure 3.4. It was constructed in three sections of 0.75" MIC6 cast aluminum such that its length is approximately equal to the 8' length of the wind tunnel test section. MIC6 aluminum is machined to a surface roughness of less than 0.50µm and a 0.005" maximum derivation from flat, a key factor for it being chosen for the splitter plate. Having a smooth fish on the splitter plate helped insure boundary layer uniformity and is easier to simulate. The splitter plate has two insert positions for a probe traverse mechanism, one upstream and one downstream of the bump location, for measuring the boundary layer profiles.

The middle aluminum section of the splitter plate is interchangeable with the bump geometry. This modular design was chosen to satisfy machining and transport constraints, and provide flexibility in later phases of the project (e.g. interchanging the flat middle section for the bump geometry), and cost. The width of the splitter plate is 0.5" less than the width of the tunnel test section. Adhesive-backed neoprene foam, 0.5" wide x 0.375" thick, was attached to both sides of the splitter plate. The total width of the plate and neoprene was wider than the test section, however the foam compressed when the test section door was closed. This ensured a tight seal on the sides of the splitter plate during testing.

A 3D printed modified super ellipse was used as the leading edge to help ensure a smooth of the laminar flow from the leading edge to the splitter plate [32]. To help ensure the flow was minimally disturbed over the leading edge, it was desired to set the flow stagnation point on the upper side of the geometric leading edge. To do this a 0.25" thick 6061 rolled aluminum trailing edge flap was attached downstream the splitter plate. Adjusting the angle of the trailing edge via a single turnbuckle would affect the location of the stagnation point on the leading edge. The leading edge has two pairs of pressure taps; each pair has one tap on the upper surface and one on the lower surface at the front of the leading edge. The difference in pressure between the upper and lower surface was used to determine the location of the stagnation point. The pairs of leading edge taps are symmetric about the centerline, in order to test for any bias.

The entire splitter plate assembly was able to be mounted at a set of precise locations in

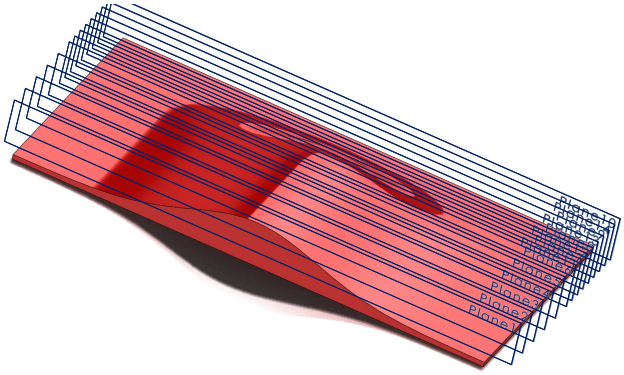

(a)

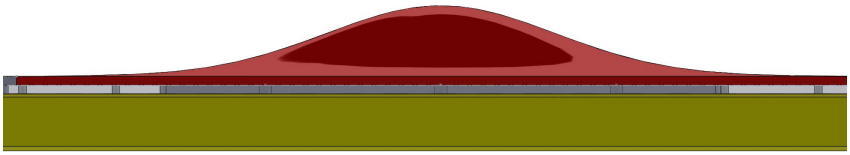

(b)

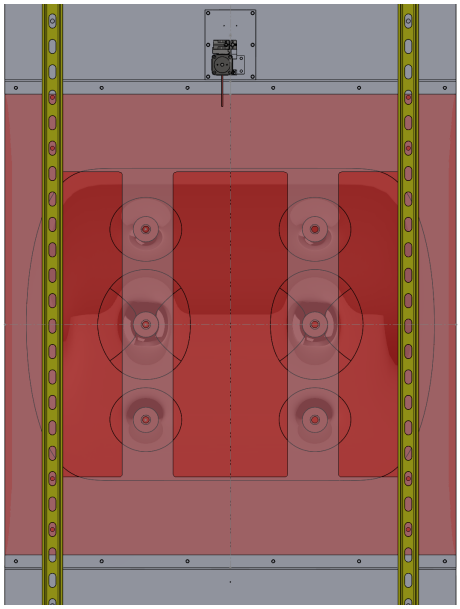

(c)

Figure 3.5: (a) Construction of 3D bump model using thirteen control planes in the half-span, upon which the Gaussian streamwise profile is explicitly enforced. (b) Rendering of the bump mounted to is 3/8" thick backing plate and splitter plate support spar. (c) Rendering of the underside of the bump, as mounted to the backing and splitter plates. The bump will be anchored with 3/8" bolts screwed into threaded inserts. The underside of the bump is hollow, such that pressure taps can be more easily mounted.

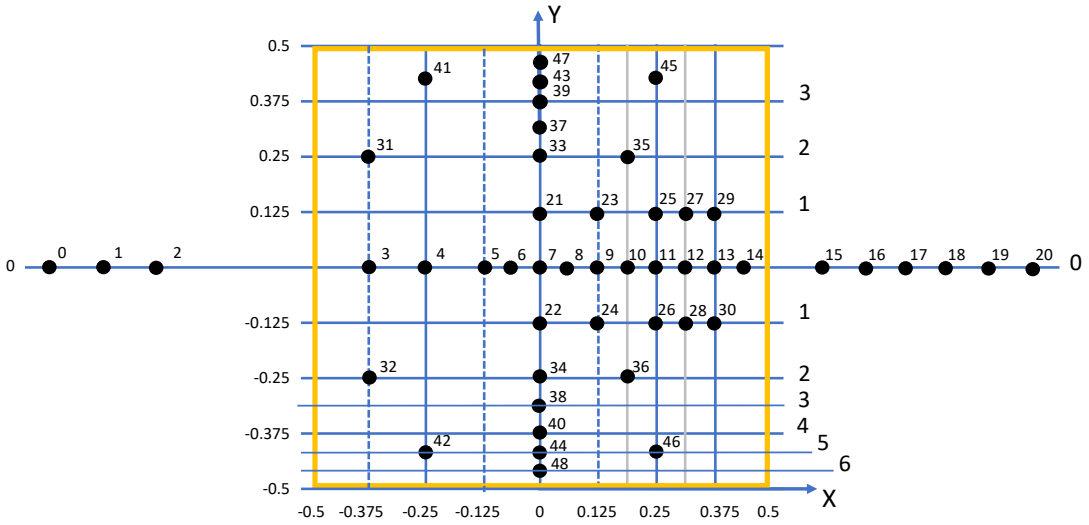

Figure 3.6: As viewed from above the bump, the figure shows pressure tap locations and numbering. Upstream is to the left. Distances are normalized by L in both the streamwise and spanwise direction. The greater concentration of pressure taps downstream is to capture more data in the separation region.

the tunnel using wall mounting inserts located at the up- and down-stream ends of the plate assembly. This was necessary for setting a precise geometry in CFD simulations.

3.2.2 Bump Geometry

The bump spanwise direction is defined by an error function with the streamwise defined by a Gaussian, see Figure 3.7. The bump geometry follows the function given in Equation 3.3, where $x_0 = 0.195L_b$, $y_0 = 0.06L_b$, $h_0 = 0.085L_b$ and z is normal to the splitter plate.

$$y(x,z) = \frac{h_0}{2} e^{-\left(\frac{x}{x_0}\right)^2} \left[1 + \text{erf}\left(\frac{\frac{L_b}{2} - 2z_0 - |z|}{z_0}\right)\right] \tag{3.3}$$

The final bump geometry was chosen to meet the goals of a high Reynolds number within facility constraints, minimizing side wall effects, and being amenable to simulation. The spanwise error function causes the bump to taper off at the spanwise edges, which minimizes the interference of side wall boundary layers. Since the splitter plate is 35.5” wide (with the foam strips of an additional 0.25” added on each side), the bump was defined in reference

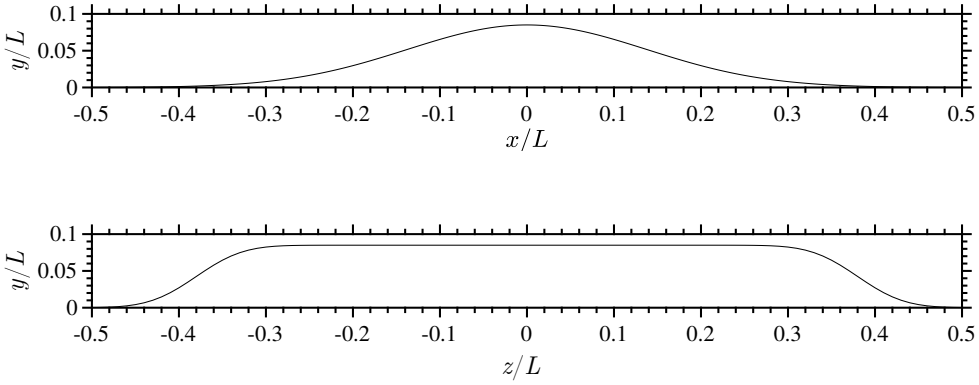

Figure 3.7: Top plot is the streamwise bump geometry in showing the smooth Gaussian. Bottom plot is spanwise geometry showing error function tapering at the side walls.

to the bump width L_b = 35.5″, instead of L, the test section width. It is important to note all results presented are relevant to L. The surface of the bump has 40 static pressure taps on the surface. See Figure 3.6 for the location of static pressure taps on the bump surface. Figure 3.8 shows the bump installed in the tunnel.

The bump was designed as a shell with minimum thickness of 0.5" along the top and 0.375" along the edges. Figure 3.5c shows six extrusions from the bump which were designed so threaded inserts could be epoxied into the underside of the bump, as shown in Figure 3.9. These thread holes were then used to secure the bump to the support plate.

A support plate made of aluminum was designed to support and secure the bump when in the tunnel. The thickness of the bump edge and the support plate were each 0.375" so that the total thickness was 0.75" to match with the splitter plate and minimize flow disturbance. The support plate was cut with a water jet to allow access to the underside of the bump and pressure taps.

The bump was manufactured with epoxy and ATH powder, by Steven Seim (steven-seim.x15@gmail.com) of CyberModelle, which was cast into a mold. A final machining pass was done to ensure final dimension. The 40 pressure taps on the bump's surface were 1/32" in diameter and normal to the surface. Given the curved nature of the surface, great care

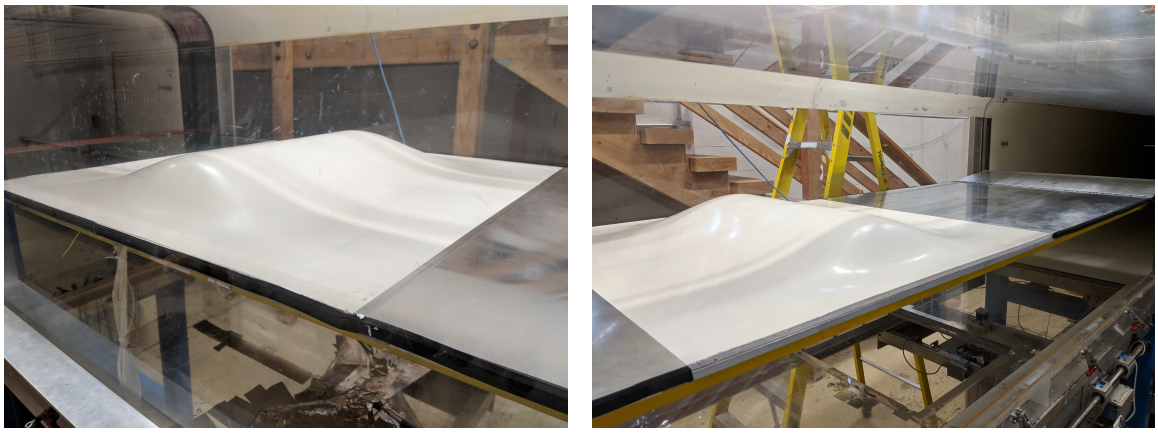

(a) (b)

Figure 3.8: Three-dimensional bump integrated into tunnel and splitter plate from (a) Looking upstream. (b) Looking downstream.

had to be taken to ensure the taps were normal. The pressure taps across the span of the ridge of the bump were drilled with a CNC. The locations of all other taps were marked with a marker in the CNC chuck. Jigs were then made such that their surface matched the bump's in a way to indicate the normal at each tap location. The taps were then carefully hand-drilled using the jig and a Dremmel tool. From the underside of the bump, 1/16" holes were drilled to be co-linear with the 1/32" tap holes. Steel tubes of 1/16" OD were then carefully epoxied on the underside. 1/16" ID tygon tubing was attached to the steel tubes for pressure measurements.

Static Pressure Measurements on Bump

Static pressure measurements were taken at 48 tap locations along the splitter plate and bump. Table A.1 in Appendix A shows all pressure tap positions with respect to L_b, the bump width. Figure 3.6 for the location of static pressure taps on the bump surface. The spanwise tap locations are symmetric about the centerline to help identify potential biases. A Baratron 226A pressure transducer, with a range of 20Torr and accuracy of 0.50%, was

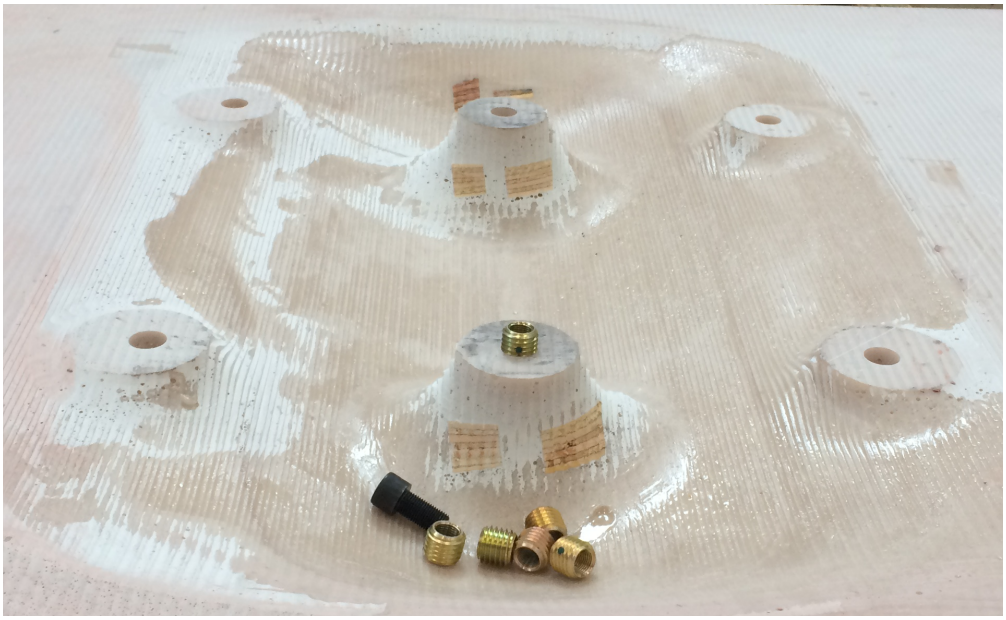

Figure 3.9: Underside of bump with one of six threaded inserts in place.

used in conjunction with a Scanivalve to measure tap pressure sequentially. The Scanivalvle solenoid valve was used to step through the pressure taps on the bump and measure the static pressure one at a time. The farthest upstream pressure tap on the plate was used as the reference and therefore attached to other side of the Baratron differential transducer.

3.3 Experimental methods

3.3.1 Boundary Layer Measurements

Splitter plate boundary layer profiles were measured with a pitot tube traverse upstream of the bump location both with and without the bump inserted. Measurements were taken at $-0.34L$, as measured in the streamwise from the top center of the bump with positive distance downstream. A highly accurate traverse was necessary given the boundary layers measured were on the order of 10mm and the pitot probe used was 0.51µm in diameter. This traverse mechanism was designed and built for this project to meet the needed requirements of high accuracy in location, a good wall datum, and minimal flow interference. Pitot pressure

data was then processed in MATLAB to calculate the boundary layer velocity profile and characteristics such as momentum thickness, θ, boundary layer thickness, δ (defined as the location where $U = .99U_\infty$).

Traverse

For the boundary layer measurements, it was necessary to have high precision (on the order of microns) for the placement of the 1/32" diameter pitot tube. A traverse with the following features was needed: 1) vertical positioning of the probe on the order of microns, 2) establish a good wall datum, 3) able to be used with other sensors (e.g. a hot-wire), and 4) able to fit in the space under the splitter plate.

Figure 3.10a shows a CAD rendering of the traverse inserted into the plate from below. The pitot tube traverse was equipped with a stepper motor that drove a lead screw with a travel distance of 1.27mm (0.05″) per full turn. The probe holder was attached to a carriage mounted to the lead screw. A Lin Engineering 417-09-18 stepper motor was used to move the slide carriage on the lead screw. The stepper motor was controlled with a R325P Single Axis Driver with 8x microstepping. A Heidenhain LS 477 SlimLine linear encoder with a step resolution of ±5µm was used to ensure high accuracy of probe location relative to starting position.

In order to know the initial wall-offset, images of the probe when closest to the wall were taken with a Nikon DSLR with a 50mm macro lens. The probe diameter in pixels was then used to determine the offset distance of the probe from the wall, see Figure 3.11 for example. Assuming the measured distances were accurate to within ±1 pixel then the calculated off-set was within 8µm.

Pitot Tube Measurements

Inserted into the traverse probe holder was a short length of 1/16" steel tubing. A 1/32" pitot tube was carefully set in the 1/16" tubing with epoxy (see Figure 3.11a.) The 1/16" tubing was fitted into the traverse probe holder by inserting it through the front probe holder

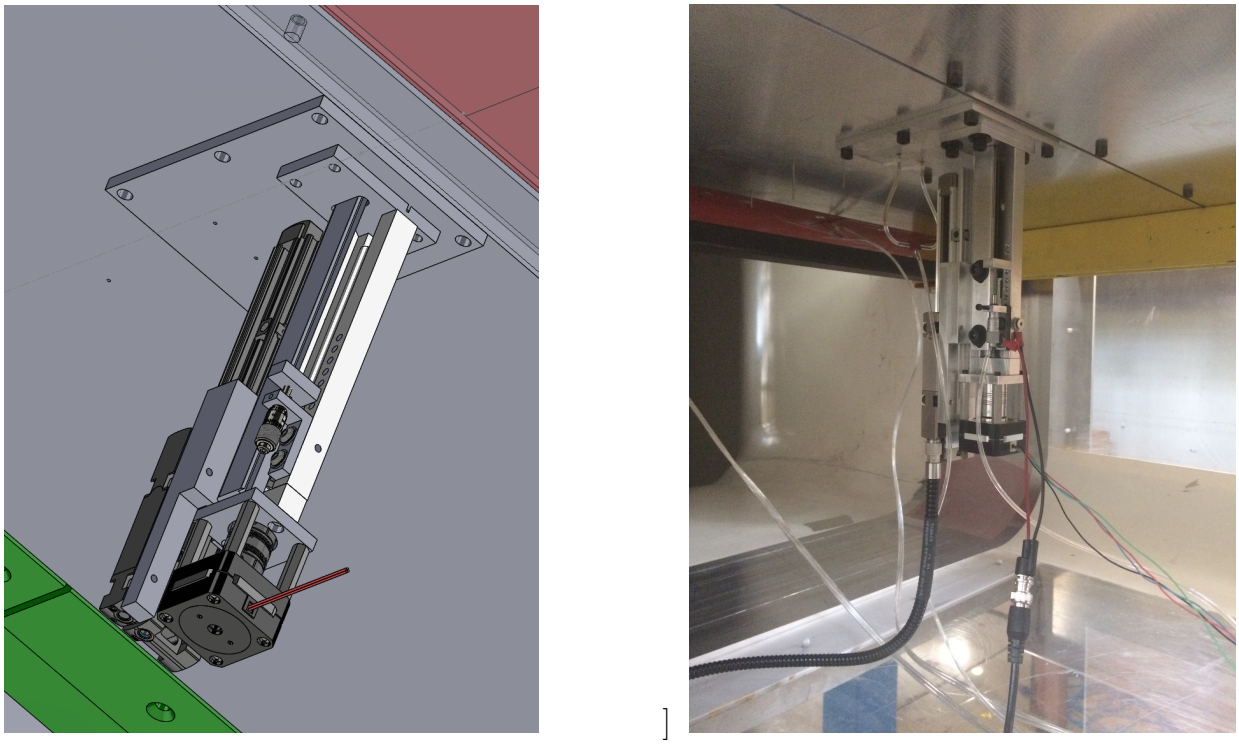

(a)] (b)

Figure 3.10: High-accuracy traversing mechanism (a) CAD render of traverse (b) traverse mounted to the splitter plate. The traverse incorporates a stepper motor driving a lead screw, with position accurately recorded with a linear encoder.

hole until about 5cm was left pointing forwards. The portion of the 1/16" tubing which had been pushed through was then bent at a right angle along the back of the probe holder. The tubing was adjusted so it rested against the back of the probe holder to allow for ease of vertical movement by the traverse.

A Baratron 226A differential pressure transducer with a range of 20Torr and accuracy of 0.50% was used with the pitot probe to measure static pressure. Two 1/32" surface pressure taps, which were inline spanwise with the pitot probe, were connected via a T-junction and used as the reference pressure.

At each vertical location, a ten second sample of the pressure was acquired. After the probe moved to the next measurement point location, the pitot was allowed time to reach a

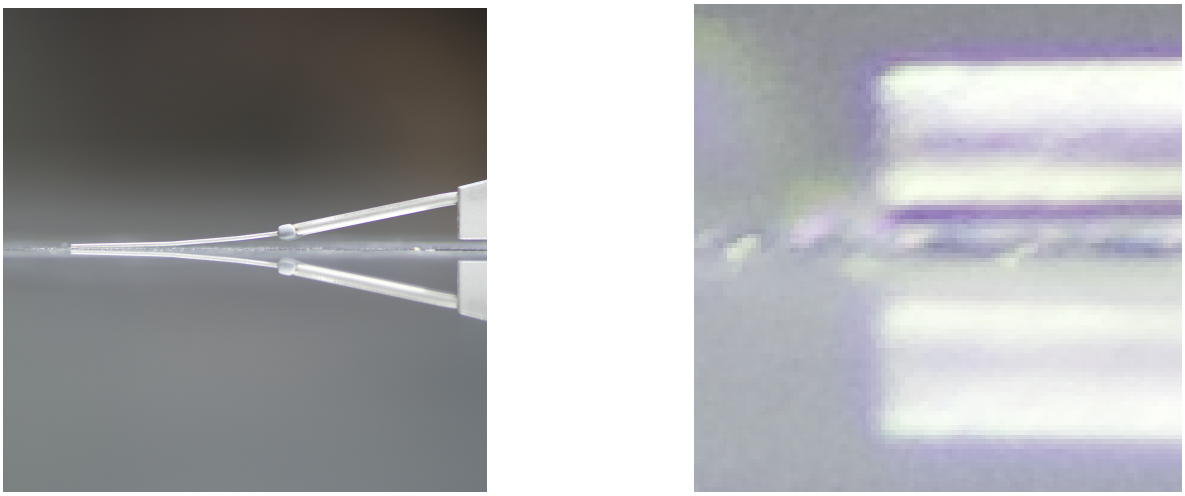

(a) (b)

Figure 3.11: An example of the images used to determine the wall-offset distance of the pitot probe. (a) Partially zoomed-in image of 1/32" pitot probe at the initial position before taking boundary layer profile data. (b) Zoomed-in image of pitot probe near wall. The pixel diameter of the probe was used to calculate the initial wall-offset distance of the probe.

steady pressure before measuring the next data point.

Pitot Tube Velocity Corrections

As illustrated in Figure 3.12, the presence of the pitot tube causes deflection of the streamlines [3]. This results in measuring the streamlines which originate at a different height than where the probe is located. The way in which streamlines are deflected varies depending on the closeness to the wall. Viscous effects can also have an impact on pitot measurements.

Corrections for near wall affects were applied using Equation 3.7, where the Reynolds number, Re_d, with a characteristic length d, probe diameter was used to correct the pressure coefficient, C_p [3]. The velocity gradient corrections were applied using Equation 3.5 with α, defined in Equation 3.6 where y is the probe centerline position from the wall [3]. For near wall corrections, Equation 3.7 was used, where $d^+ = \frac{dU_\tau}{\nu}$ is the non-dimensional pitot diameter, U_τ is the sheer velocity at the wall, and ν is the kinematic viscosity [3]. The velocity gradient

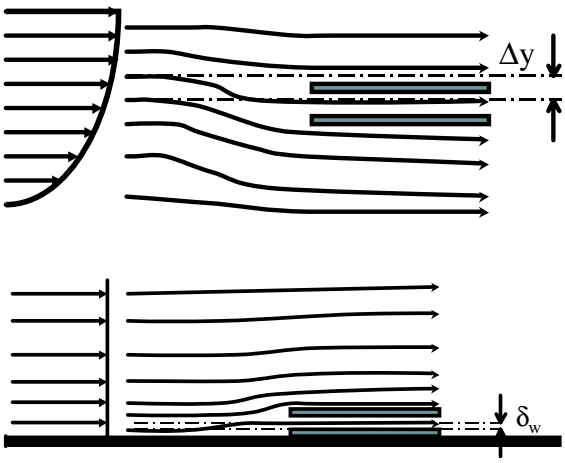

Figure 3.12: Pitot affect on streamlines. Upper portion shows affect on shear flow, which causes mis-measuring of the velocity gradient. Lower portion shows affect on uniform near wall flow. Figure credit [3].

and near wall corrections are both meant to correct the position of measurements. The velocity gradient correction does this by adjusting the velocity associated with a measured position (thus "correcting" the velocity instead of the position directly). While the near-wall correction directly adjusts the position of the probe. Figure 3.13 shows the difference between corrected and uncorrected boundary layer profiles for the 30m/s. 240-grit case.

$$C_p = 1 + \frac{10}{Re_d^{1.5}} \tag{3.4}$$

$$\frac{\Delta y}{d} = 0.15\tanh(4\sqrt{\alpha}) \tag{3.5}$$

$$\alpha = \frac{d}{2U(y)}\frac{\mathrm{d}U}{\mathrm{d}y} \tag{3.6}$$

$$\frac{\delta_w}{d} = \begin{cases} 0.150 & d^+ < 8 \\ 0.120 & 8 < d^+ < 110 \\ 0.085 & 110 < d^+ < 1600 \end{cases} \tag{3.7}$$

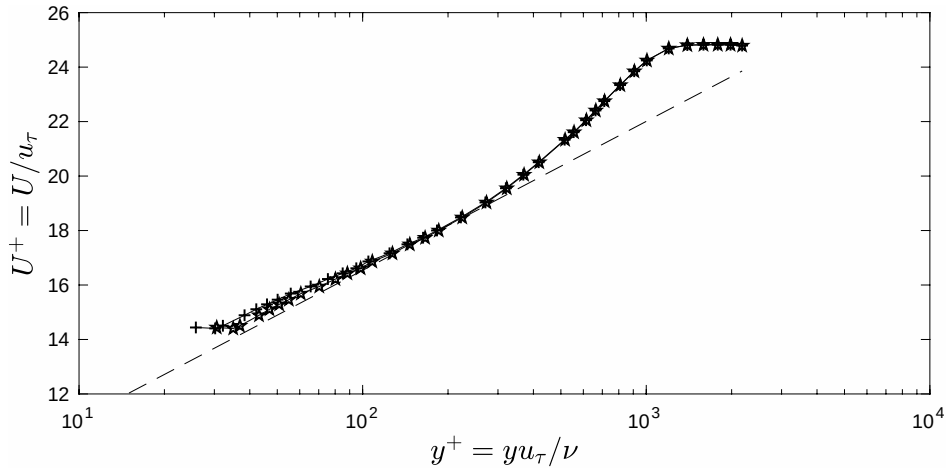

Figure 3.13: Effect of viscous and shear corrections to near-wall velocity profile (240-grit, 30m/s, no bump). + Uncorrected, ☆ Corrected. Dashed lines indicate log-law with $\kappa = 0.421$ and intercept $B = 5.6$.

3.3.2 Flow Visualization

China clay surface flow visualization is a useful qualitative tool for studying flow movement near a solid surface. A liquid mixture with small particles (e.g. china clay) is painted on the model before a test. Once the tunnel is turned on, the mixture flows over the model with the small particles following the streamlines. As the liquid portion of the mixture evaporates, the particles are left behind and the model can be photographed. This produces an image of the flow surface streamlines, which can then be examined in greater detail.

For this project china clay flow visualization was used to study the structure of the separation bubble formed downstream of the bump. The china clay mixture and black light were provided by Kristin Wind Tunnel at the University of Washington. The china clay mixture was five parts kerosene, one part Kentucky ball clay, and one part yellow Day-Glo powder, which fluoresced when under a black light making the streamlines more clear.

The china clay mixture was painted onto the bump, the tunnel was turned on and, once the test velocity was reached, continued to operate at the test velocity while the kerosene evaporated. Once the kerosene evaporated, only the china clay and Day-Glo powder re-

mained, following surface streamlines. The bump was then photographed under a black light from above and downstream, with the camera angled upstream. Pictures were acquired using A Nikon DSLR with an 18mm lens mounted to the test section framing. To allow for more control in picture quality, the author was atop the test section to be able to inspect images and adjust camera settings throughout each test, as needed. Tests were conducted at night and with portions of the test section blacked-out in order to minimize light interference. See Figure 3.14 for view of the bump set-up seen through side of the test section.

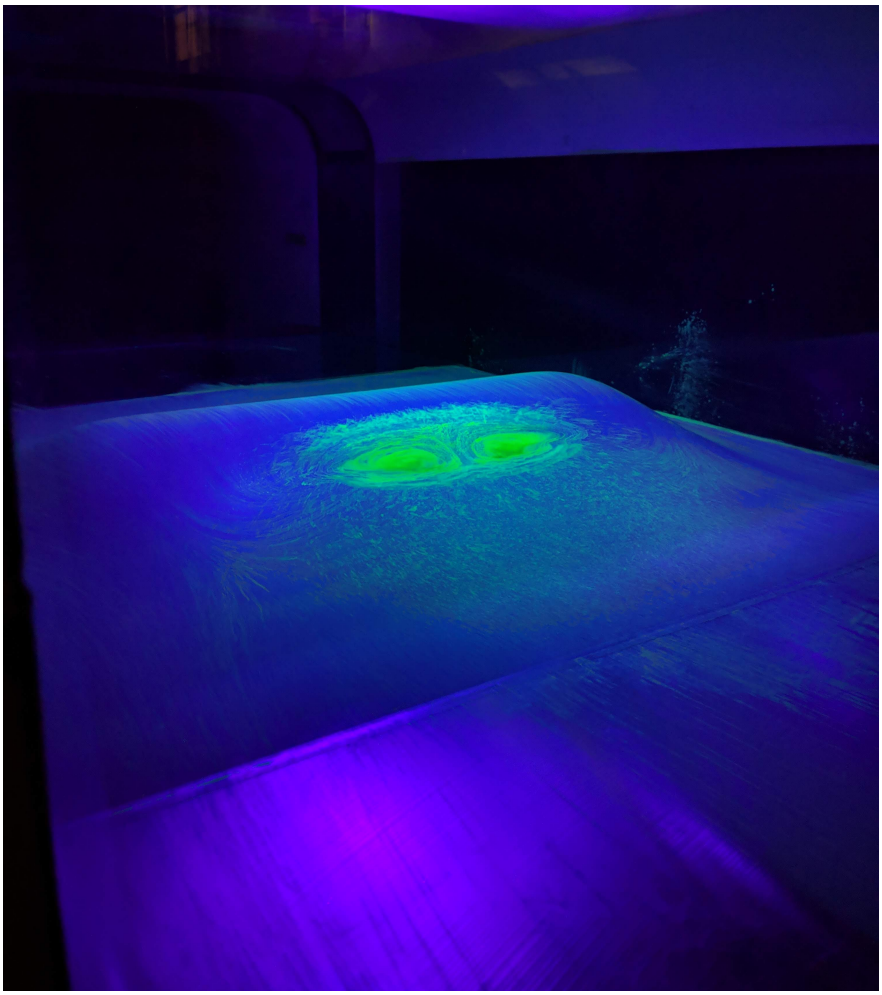

Figure 3.14: Bump viewed downstream through the test section side window during flow visualization test.

Image Corrections Applied

Due to the camera angle needed to clearly capture the desired bump area, the raw photos had noticeable distortions. Keystone and barrel distortion corrections were applied in Adobe Photoshop using a Lens Correction filter. The photos were cropped to the dimensions of the bump, resulting in a uniform scale in both directions across images. A sample image from each test set was corrected, cropped, and editing settings saved. The editing settings were then applied to all images in the test set using the Batch feature in Photoshop. In an effort to increase visibility of flow features, the images were further post-processed to eliminate all but green coloring and adjust their contrast and brightness. Dashed red lines were added to show the stream and spanwise centerlines of the bump. See Figure 3.15 for comparison of corrected and uncorrected images.

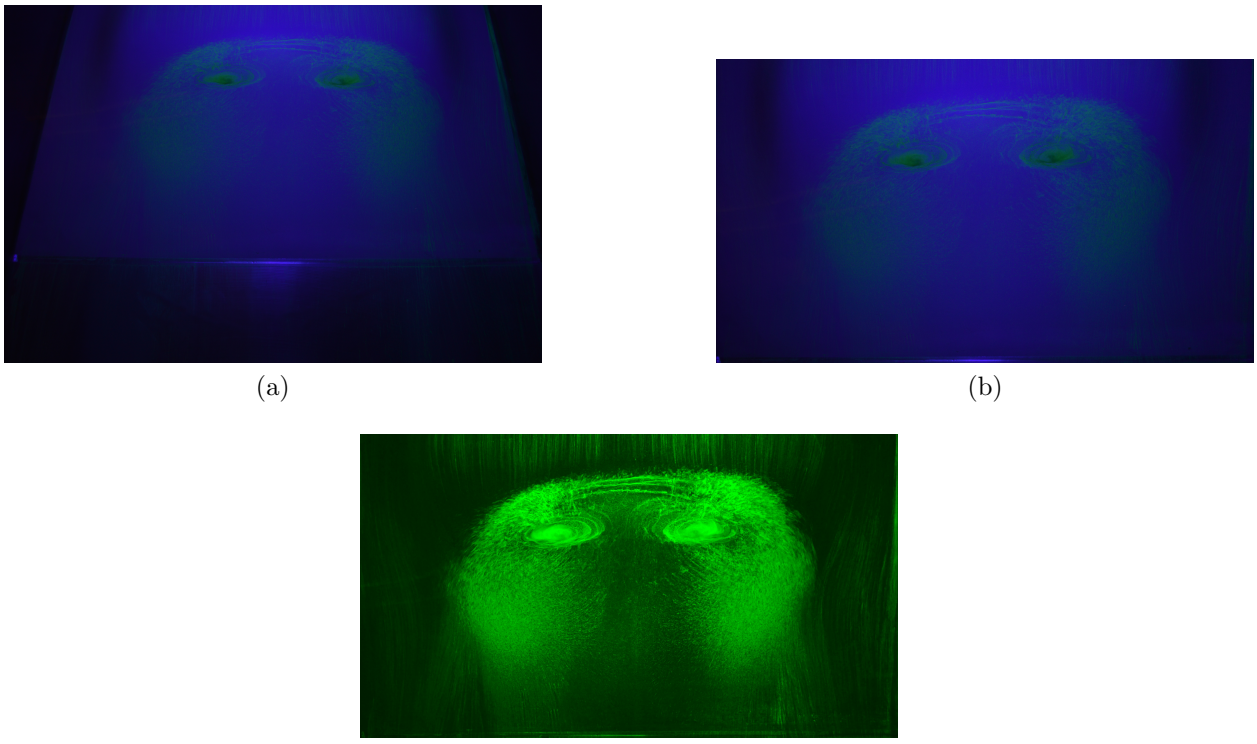

(a) (b)

(c)

Figure 3.15: An example showing the differences between the (a) uncorrected, (b) perspective corrected and (c) both perspective and color correction applied to a china clay photo.

Chapter 4

RESULTS AND DISCUSSION

4.1 Tunnel Qualification

4.1.1 Freestream Turbulence

Figure 4.1 shows the freestream turbulence (u_{rms}/U_∞) across the velocity range of the tunnel (10 to 60m/s). The upper and lower bounds of the freestream turbulence are 0.13 and 0.34%. Upon examination of the turbulence spectrum, Figure 4.2, there are clear spikes at harmonics of 60Hz. This suggests noise due to power in the signal. It is hard to say how much of the freestream turbulence measured is actually freestream turbulence and how much is due to the noise from power in the signal. Based on a range of tests, the freestream turbulence averaged 0.2%, which is acceptable for the other tests in this study. The freestream turbulence is likely much better than this and reduction of signal noise from power sources is being looked into for future tests.

4.1.2 Tunnel Uniformity

Overall, the 3'x3' tunnel showed good mean uniformity in both the vertical (Figure 4.3a) and horizontal directions (Figure 4.3b). All three velocities, U_1 = 20m/s, U_2 = 45m/s, and U_3 = 60m/s, show uniformity relative to the mean downstream stationary pitot tube velocity, U_∞.

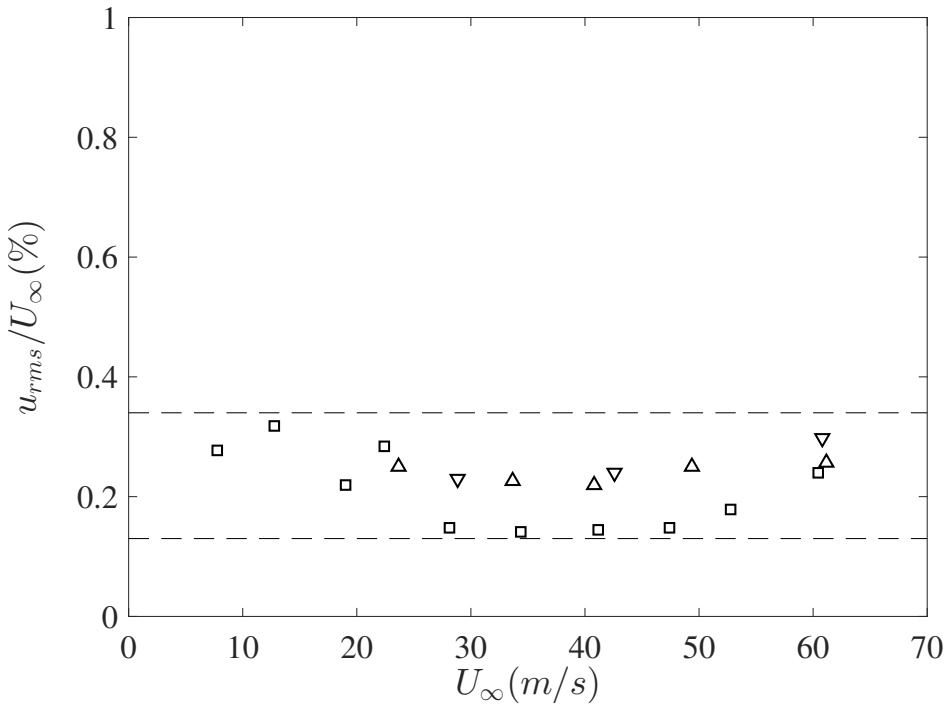

Figure 4.1: Freestream turbulence intensity. Dashed lines indicate range of values between 0.13 and 0.34%.

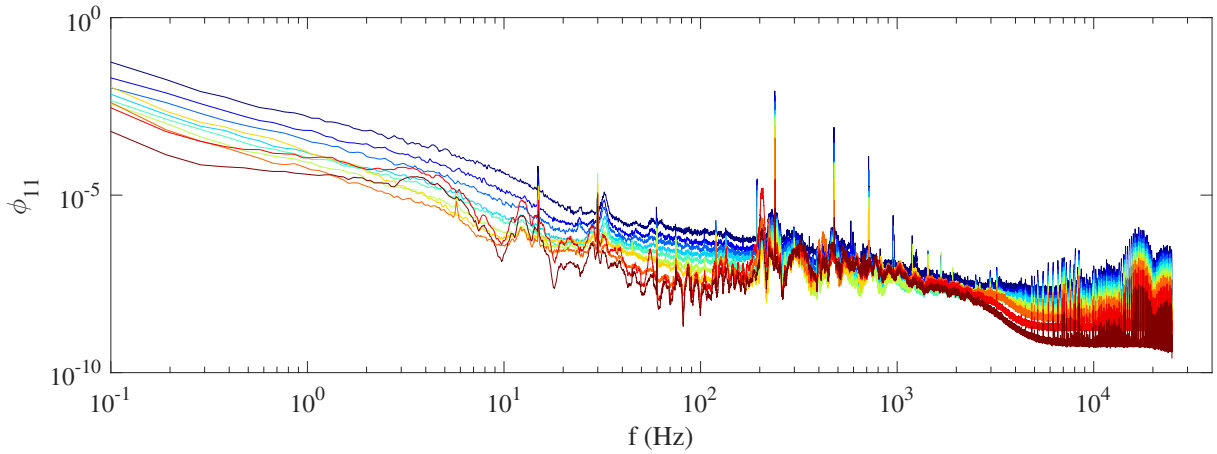

Figure 4.2: Freestream turbulence spectrum. Clear spikes are seen at hormonic frequencies of 60Hz, indicating electrical noise in the signal.

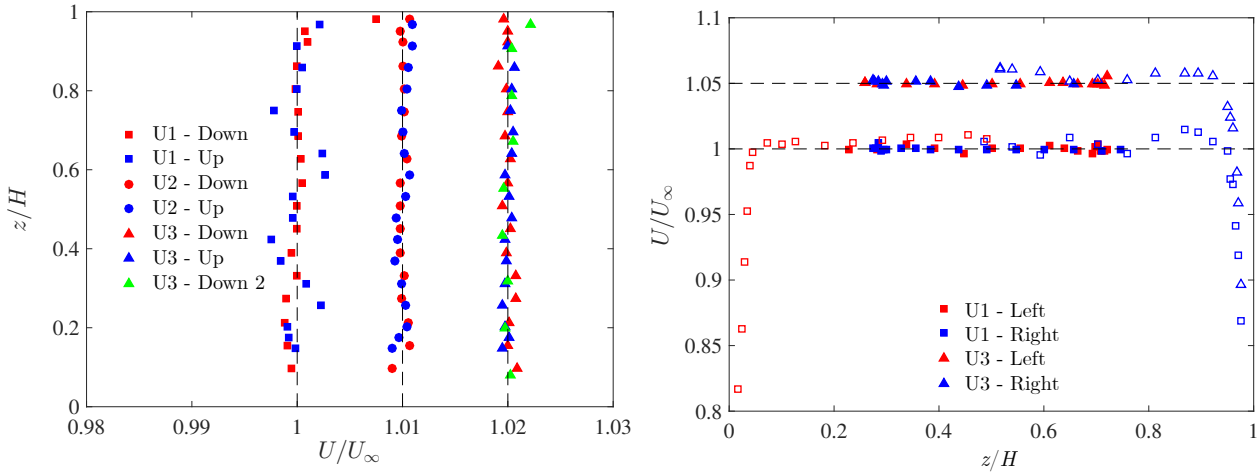

(a) (b)

Figure 4.3: Examination of (a) vertical and (b) horizontal mean streamwise velocity uniformity at the center of the test section. $U_1 = 20$m/s (square), $U_2 = 45$m/s (circle), $U_3 = 60$m/s (triangle). Closed and open symbols represent pitot tube and hot-wire data, respectively. Note change in ordinate for each tunnel velocity. Left side of tunnel has the test-section access door, thus restricting access close to the side wall.

4.2 Splitter Plate Boundary Layer Qualification

4.2.1 Flat Plate Configuration

The incoming flow was studied in the absence of the bump. The leading edge stagnation point was set as to ensure that it was above the geometric leading edge. This was done so the flow before the trip did not have any large disturbances present. Splitter plate qualification tests were conducted at 30 and 60m/s with trips of 1mm thick velcro, 60-, 120-, and 240-grit sandpaper. All sandpaper trips were 1" wide in the streamwise direction, while the velcro was 0.5" wide. Conditions and results are summarized in Table 4.1. Overall, the flow exhibited behavior of a canonical turbulent boundary layer in all test cases and trips except the 30m/s un-tripped case, which was transitional.

Config.	Trip	Size	U_∞ [m/s]	δ [mm]	h/δ	C_f $\times 10^3$	Re_θ	Re_τ	ΔU^+	Sym.
No Bump	None	-	30	5.1	15.1	-	1100	-	-	○
		-	60	9.4	8.3	3.2	3000	1431	1.93	●
	Sandpaper	240-grit	30	14.7	5.3	3.2	3000	1152	2.24	☆
			60	12.3	6.3	2.9	5000	1778	2.61	★
		120-grit	30	15.3	5.1	3.3	3000	1215	1.92	□
			60	14.7	5.3	2.8	5800	2082	2.61	■
		60-grit	30	16.4	4.8	3.2	3500	1321	2.14	△
			60	15.1	5.1	2.9	5800	2158	2.38	▲
	Velcro	$\sim 1mm$	60	15.2	5.1	2.9	5700	2166	2.34	▼
With Bump	Sandpaper	240-grit	30	13.7	5.7	3.4	2800	1149	1.83	◊
			60	12.4	6.2	2.9	4900	1765	2.52	♦

Table 4.1: Test conditions for splitter plate boundary layer for all tripping devices. U_∞ is the freestream velocity, δ is the 99% thickness of the boundary layer, h is the height of the bump, Re_θ and Re_τ are the momentum thickness and friction Reynolds numbers, and ΔU^+ is the maximum deviation of the mean velocity from the log-law in the outer layer. The plate width Reynolds number of 30 and 60m/s cases was $Re_L = 1.8 \times 10^6, 3.6 \times 10^6$, respectively.

Leading Edge Stagnation Point

The leading edge stagnation point was positioned to be above the geometric leading edge. This was achieved by adjusting the trailing edge flap. Due to the traverse mechanism, cables, and pressure tubing underneath the plate, the splitter plate stagnation point could be under the leading edge without the adjustment of the flap. This could cause unsteadiness in the leading edge flow and affect uniformity. The pressure difference between the two sets of taps on the upper and lower side of the leading edge were measured while varying the trailing edge flap angle. Figure 4.4 shows a higher trailing-edge angle moved the leading edge stagnation point upwards on the leading edge. Figure 4.4 is for the flat plate configuration. Since a $C_p > 0$ was desired, a trailing edge flap angle of seven degrees was set for all subsequent tests.

The leading edge C_p was remeasured with the bump present, however the presence of the bump seemed to show no affect on the location of the leading edge stagnation point. For all tests with the bump present, the trailing edge flap was set to seven degrees.

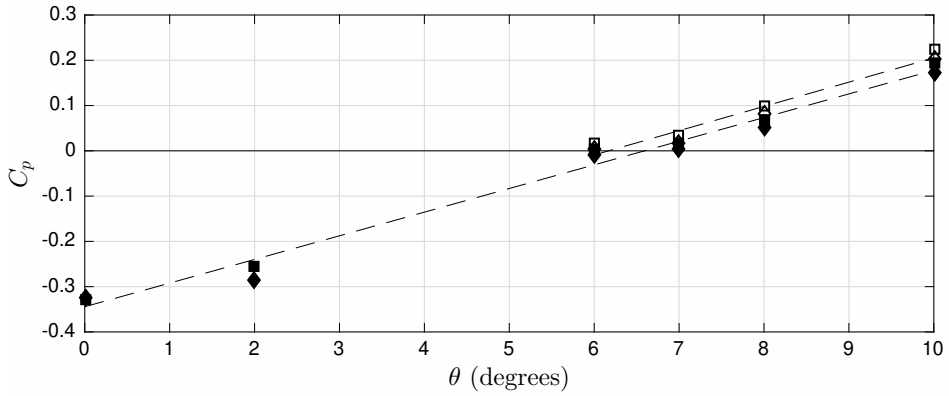

Figure 4.4: Angle of trailing edge flap and its affect on C_p at the leading edge. Positive C_p indicates stagnation point on topside of leading edge, as desired. Open and closed symbols for 30 and 60m/s, respectively. Data for flat plate configuration. Squares and diamonds represent tap pairs to the right and left of the centerline, respectively.

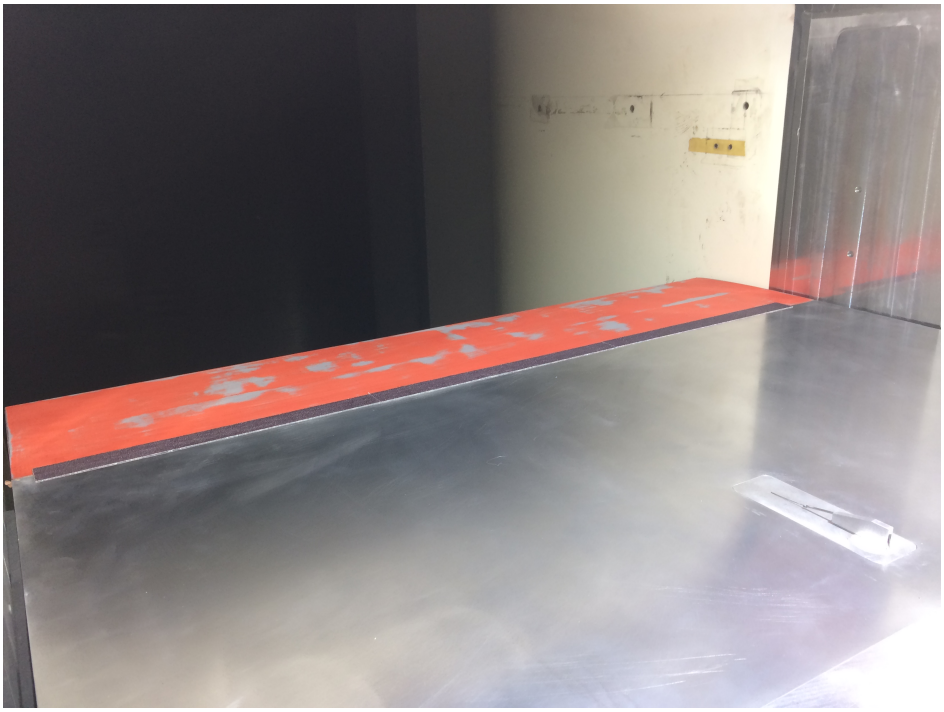

Figure 4.5: Upstream portion of the splitter plate with tripping device at the transition of the leading edge and main portion of the splitter plate.

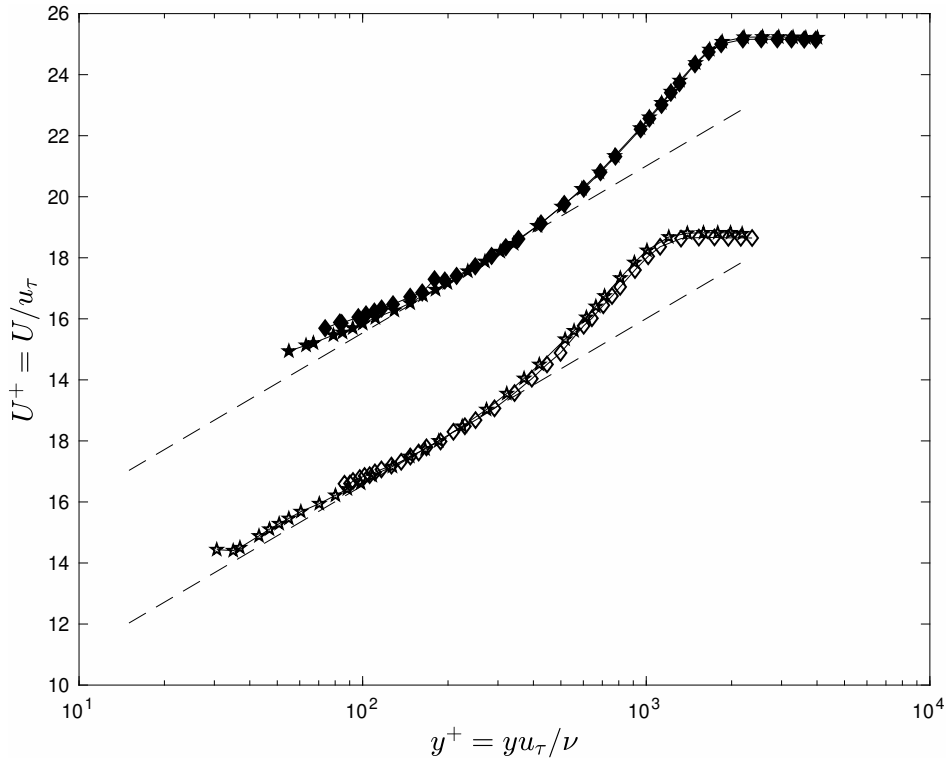

Figure 4.6: Comparison of inner-scaled mean velocity profiles, with and without the bump present. Symbols as in Table Table 4.1. Note shift in ordinate of 5 units for 60m/s cases (filled symbols). Dashed lines indicate log-law with $\kappa = 0.421$ and intercept $B = 5.6$.

4.2.2 Effect of tripping devices of splitter plate boundary layer development

A range of tripping devices were tested to ensure a fully developed boundary layer upstream of the bump and consistent development length for the range of test velocities. Test cases of no trip, sandpaper of 60-, 120-, 240-grit, and velcro, were studied for the plate prior to inserting the bump geometry. Strips of self-adhesive sandpaper or velcro were placed at the transition between the leading edge and the upstream plate section, see Figure 4.5. All trip test cases were done at 30 and 60m/s. Conditions and calculated results are presented in Table 4.1.

Figure 4.7 shows the log-law plot of the boundary layer for all trips using inner coordinates, with the exception of the untripped 30m/s case, which was transitional. The Clauser

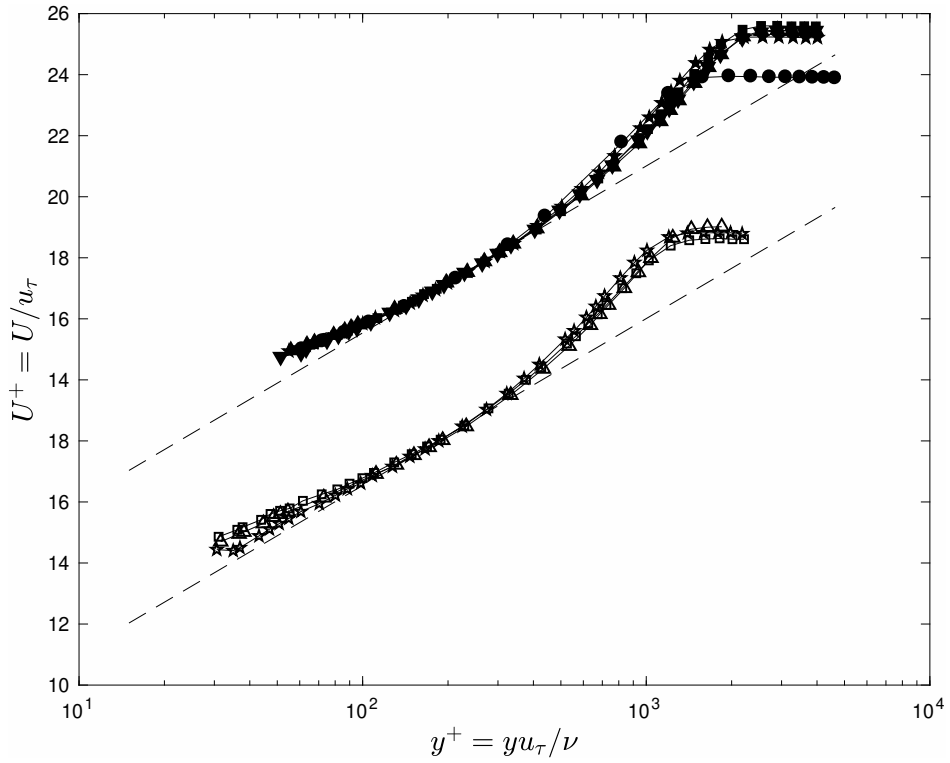

Figure 4.7: Variation in inner-scaled mean velocity profile for different tripping devices. Symbols as in Table 4.1. Note shift in ordinate of 5 units for 60m/s cases (filled symbols). Dashed lines indicate log-law with $\kappa = 0.421$ and intercept $B = 5.6$.

chart method [33] was used to find the friction velocity, $u_\tau = \sqrt{\tau_w/\rho}$, where a portion of the mean velocity profile was fitted to the log-law with $\kappa = 0.421$ and $B = 5.6$. While most of the near-wall region lies on the log-law line, even after applying the corrections outlined in Section 3.3.1, there is a portion which does not. This is most likely due to deformation of the 1/32" probe. Very similar boundary layer profiles are produced regardless of tripping device. As a result, it was decided to use the smallest trip, 240-grit, for all subsequent tests. A comparison of boundary layer profiles with the 240-grit trip, with and without the bump, as shown in, Figure 4.6, reveals the the flow does not appear to be affected by the presence of the bump downstream.

The maximum deviation from the log-low can indicate either over- or under-tripping of

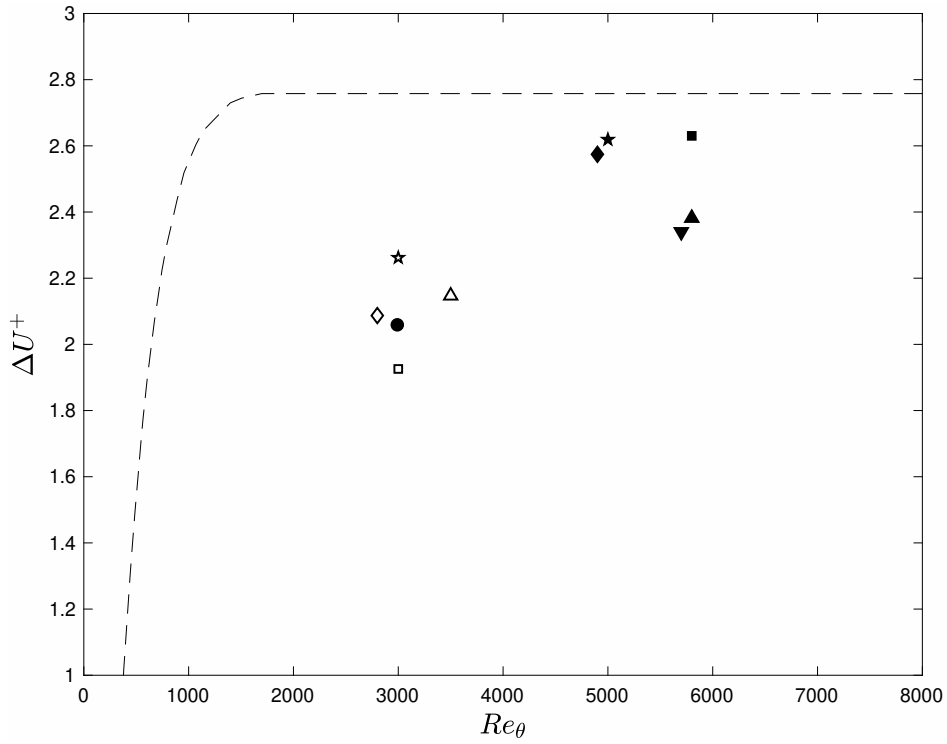

Figure 4.8: Variation the maximum deviation of mean velocity profiles from the log-law in the outer layer, ΔU^+, called the wake size. Results are compared with the correlation of Coles [4], indicated with a dashed line. Symbols as in Table.

the boundary layer and therefore a continued influence from the initial conditions, as shown by Coles [4]. The maximum deviation is calculated using Equation 4.1.

$$\Delta U^+ = max\left[U^+ - \frac{1}{\kappa}\ln\frac{yu_\tau}{\nu} - B\right] \quad \text{for} \quad y/\delta > 0.2. \tag{4.1}$$

Figure 4.8 shows the maximum deviation in the wake as a function of Re_θ for all tripping devices at 30 and 60m/s and Coles' correlation for the boundary layer wake deviation for a correctly tripped boundary layer. The 60m/s cases compare well with the expected wake deviation. All 30m/s cases are lower than expected, however. Difficultly in estimating friction velocity for the 30m/s cases, due to the near-wall deviation, might have affected the maximum wake deviation.

	Set Name	Re_L ($\times 10^6$)	Re_h ($\times 10^3$)	Ma	H/L	$C_f \times 10^3$	h/δ	h/θ	Vis.	Press.
UW	10m/s	0.69	58.0	0.034	0.5	-	-	-		✓
	20m/s	1.19	99.5	0.058	0.5	-	-			✓
	30m/s	1.80	151	0.087	0.5	3.4	5.7	52.7	✓	✓
	40m/s	2.40	201	0.12	0.5	-	-	-	✓	✓
	50m/s	3.00	251	0.15	0.5	-	-	-	✓	✓
	60m/s	3.60	301	0.17	0.5	2.9	6.2	61.8	✓	✓
	SA RC - 2D	0.586	49.1	-	0.5	10.6	4.7	41.6		✓
	SA RC - 2D	1.17	98.2	-	0.5	9.3	5.2	48.8		✓
	SA RC - 2D	1.76	147	-	0.5	8.6	5.5	48.9		✓
	SA RC - 2D	3.51	294	-	0.5	7.8	5.9	53.9		✓

Table 4.2: Test conditions for flow visualization and static surface pressure. Conditions for SARC-2D simulations by Maddie Samuell [5] are also shown. Note the overlap in Re_h, h/δ, and h/θ between experiments and simulations.

4.3 Separated Flow Over Bump Test Geometry

Both flow visualization and surface static pressure measurements were conducted to study the separated region of the flow downstream of the bump. Table 4.2 shows the parameters for both the experimental and corresponding 2D RANS simulations conducted by Maddie Samuell [5].

4.3.1 Bump Flow Visualization

Figure 4.9 shows enhanced images of china clay flow visualization on the downstream potion of the bump for velocities between 30 and 60m/s and with different amounts of china clay mixture applied for the same test. Red dashed lines have been added to indicate the streamwise and spanwise centerlines of the bump. The enhanced images of Figure 4.9 show surface streamlines. This is most clear for the highest velocities. At all velocities, a separated region surrounded by two surface vortices appears to be present.

The flow visualization seems to suggest the vortices move closer together at lower velocities, and therefore that the separated region narrows. The location of the most upstream separation point seems to be constant with velocity, within uncertainty. A saddle point is visible in some images, such as Figure 4.10, indicating reattachment of the boundary layer. No trend in reattachment location could be detected with this method for the range of Reynolds number tested.

Pools of fluid can be seen at the vortex cores for the different velocities. These pools would have sputtering droplets "jumping" out of them and landing elsewhere on the model. This would decrease the clarity of the separation line and other flow structures. Higher velocity flows had smaller pools of liquid in the vortex cores than the lower velocities. The pools of liquid were probably less likely to form due to the higher velocity moving the liquid more effectively over the bump.

Lower velocities proved harder to visualize with the clay mixture. At 30m/s, pool of clay mixture would form in the separated region resulting in only one structure being visible. This pool would sputter clay mixture and require longer runs in order to evaporate the kerosene and leave behind photographable clay. Most likely due to the size of the pool of liquid and the resultant sputtering, less detailed structure was visible with the resulting flow pattern. Lower velocities were also likely to be more susceptible to gravity pulling the clay mixture downhill on the bump. At higher velocities, the flow was likely able to counter gravity better and keep the clay mixture in the vortex cores. Lower velocities did show more distinct surface

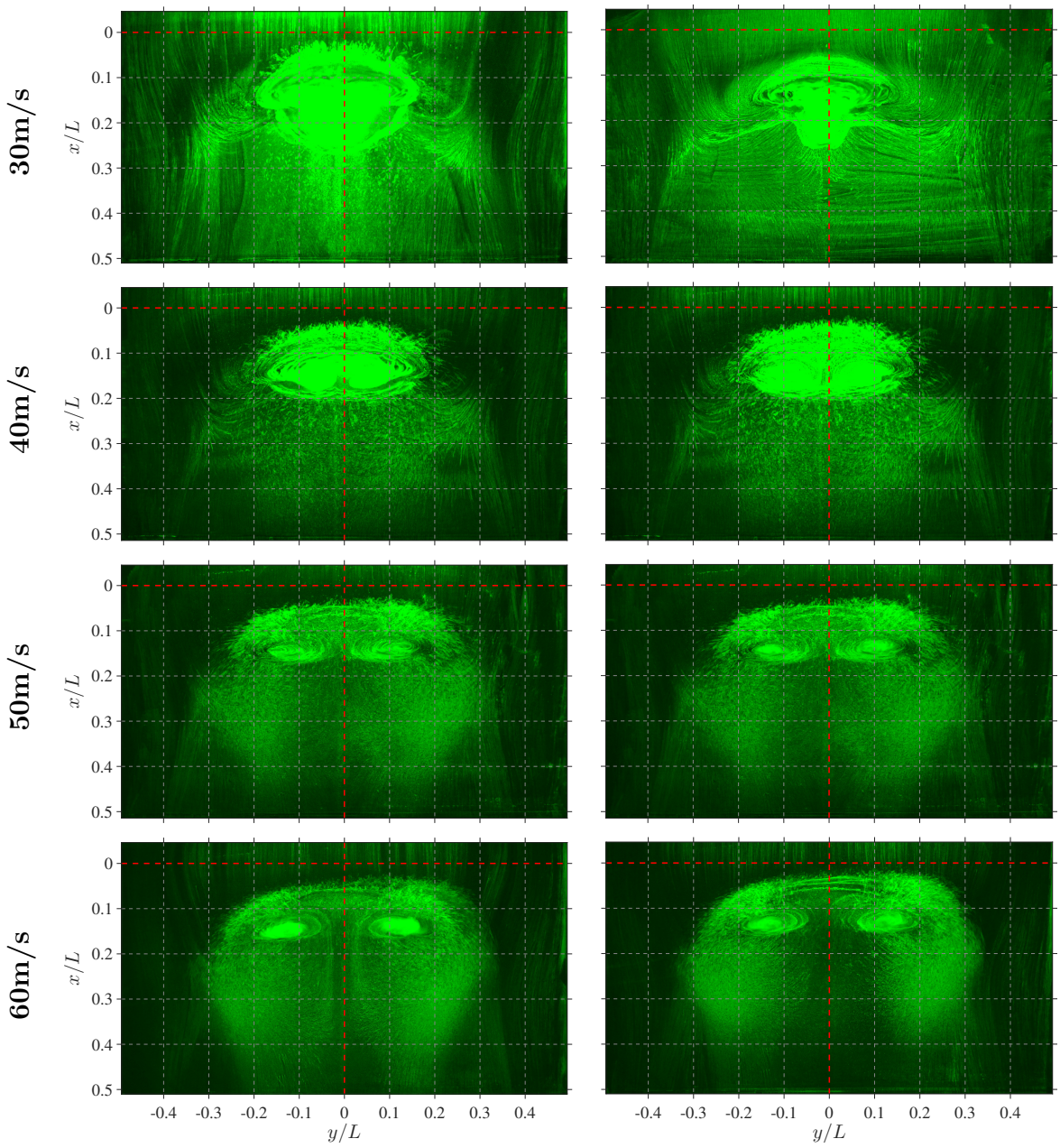

Figure 4.9: China clay surface flow images at four freestream velocities. Left and right columns are different realizations of the same test, using different quantities of clay. The centerline of the bump in both streamwise and spanwise directions is indicated with red dashed lines. Top of the images is the upstream direction.

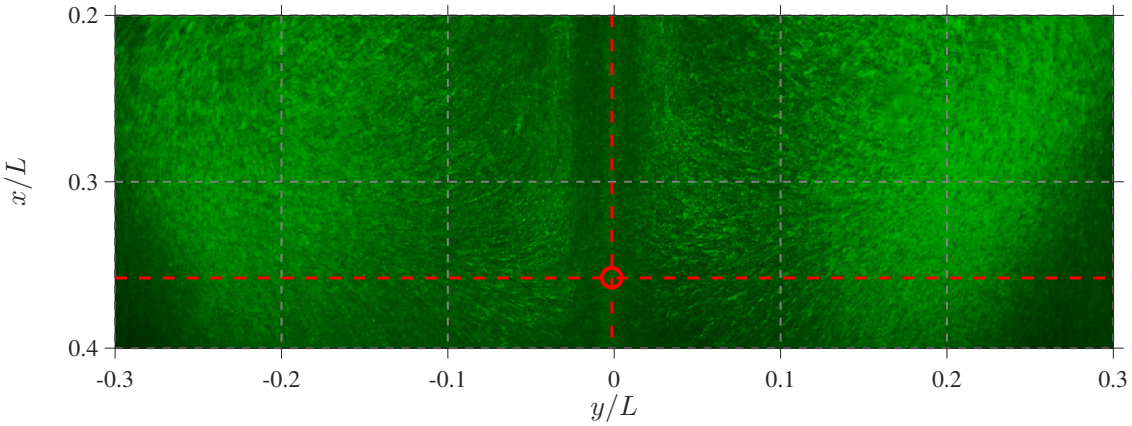

Figure 4.10: Highlight of saddle point for 60m/s case.

streamlines outside of the separated region than higher velocity tests.

The flow visualization shows a well defined region of separation on the downstream side of the bump at the macro scale. Key structures are visible, such as surface vortices, separation line, and a saddle point. This information is useful for informing further investigations of the separated region.

4.3.2 Static Pressure Measurements over Bump Surface

Surface pressure data were experimentally measured and compared to simulated surface pressure data. The simulation data are from a two-dimensional RANS model conducted by PhD student Maddie Samuell [5]. Samuell used a Spalart-Allmaras one-equation model with rotation and curvature correction [34]. Using Schlichting's correlation [35], Equation 4.2, the experimental momentum thickness Reynolds number, Re_θ, was used to calculate the inflow length of the simulation, x, through the simulation Re_x value. The inflow length for the model was set to $1.5L$, as found from Equation 4.2. This ensured an equivalently developed boundary layer between the experiments and the simulations.

$$Re_\theta = 0.036 Re_x^{0.8} \tag{4.2}$$

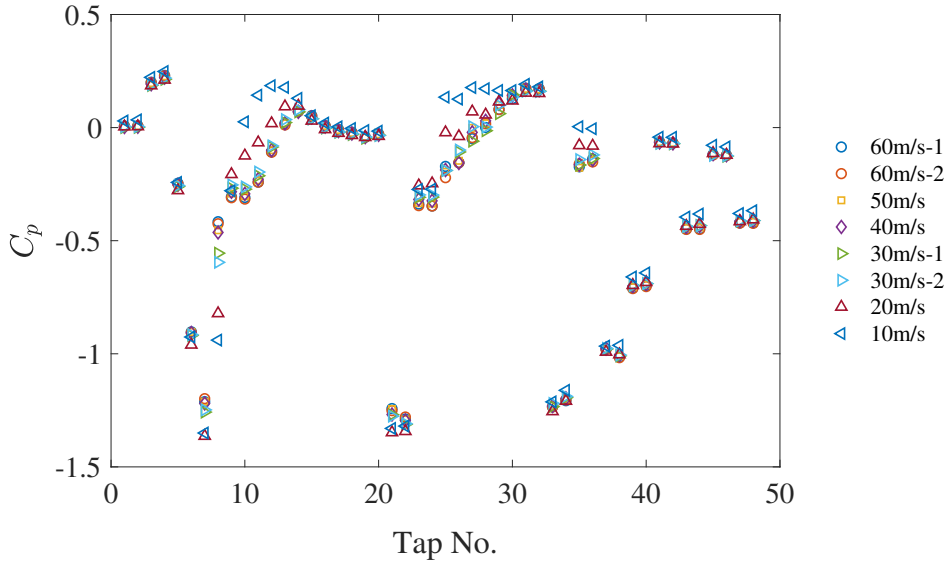

Figure 4.11: Survey of all pressure coefficient data from current experiments. Tap numbers correspond to locations in Figure 3.6.

Two other parameters which were similar between the experiments and simulations are h/δ and h/θ, where δ is boundary layer thickness and θ is the momentum thickness. Flow separation is related to how much momentum is in the boundary layer, therefore using h/θ to match the simulation accounts for this importance in the simulations. Having h/δ be within the same range for the experiments and simulations is another way to show the boundary layers are equivalent. By using h/δ and h/θ, instead of just δ and θ, there is a known and important shared length scale of h, the height of the bump.

All experimental pressure data are presented in Figure 4.11 by tap number. Spanwise symmetric pairs (taps 21 through 48, see Figure 3.6) show the flow is symmetric about the centerline. Figure 4.11 also shows data from two 30 and 60m/s tests, which match well, showing good repeatability of the results. For velocities over 30m/s, there seems to be no variation in surface pressure with Reynolds number.

Figure 4.12 shows the centerline pressure data from experiments and the 2D RANS simulations conducted by Maddie Samuell [5]. Outside of the separated region, there is close

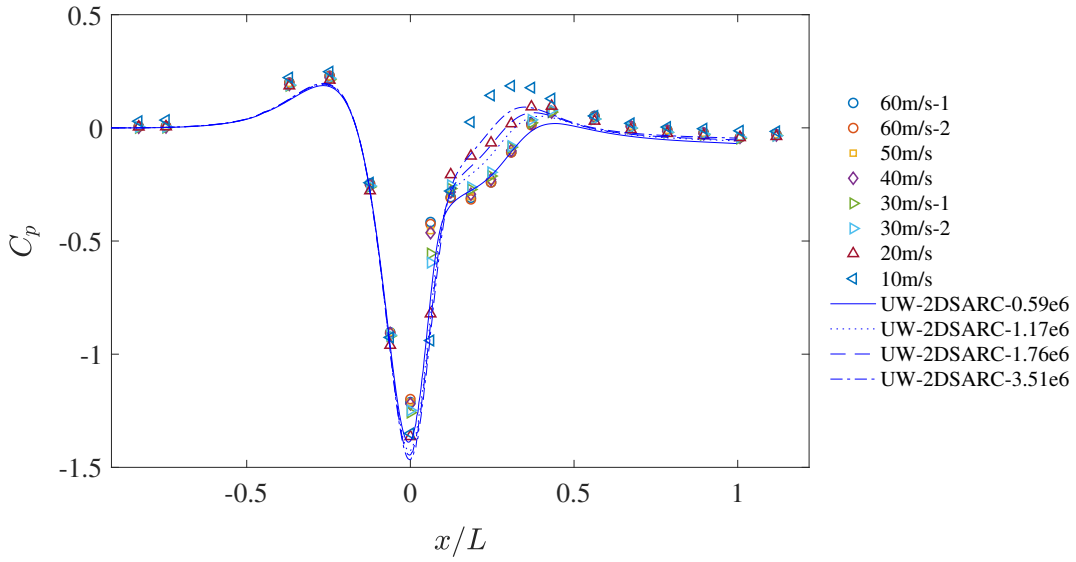

Figure 4.12: Variation in pressure along the streamwise centerline. Reference pressure has been taken at the location of the most upstream tap.

agreement across all Reynolds numbers, for both the experiments and simulations. The recovery region over the bump along the centerline, shown in Figure 4.13, shows there is little variation among the experimental data for velocities above 30m/s. The simulation pressures are within bounds of the measured values in this region. The experiment and 2D RANS model data match closely across Reynolds number in the non-separated region. However, the 2D-SARC data show a Reynolds number trend opposite of the one observed in the experimental data.

The variation in pressure along the spanwise ridge of the bump is shown in Figure 4.14. There is general agreement among the pressures for all tests. However, right at the center, there does appear to be a slight rise in pressure at higher Reynolds numbers.This suggest some amount of three-dimensionality all the way to the centerline. Such three-dimensionality might also be difficult to capture with current simulations.

In considering how the experimental surface pressure data and flow visualization compare, the flow visualization proved difficult to interpret. Overall, the surface pressure data is

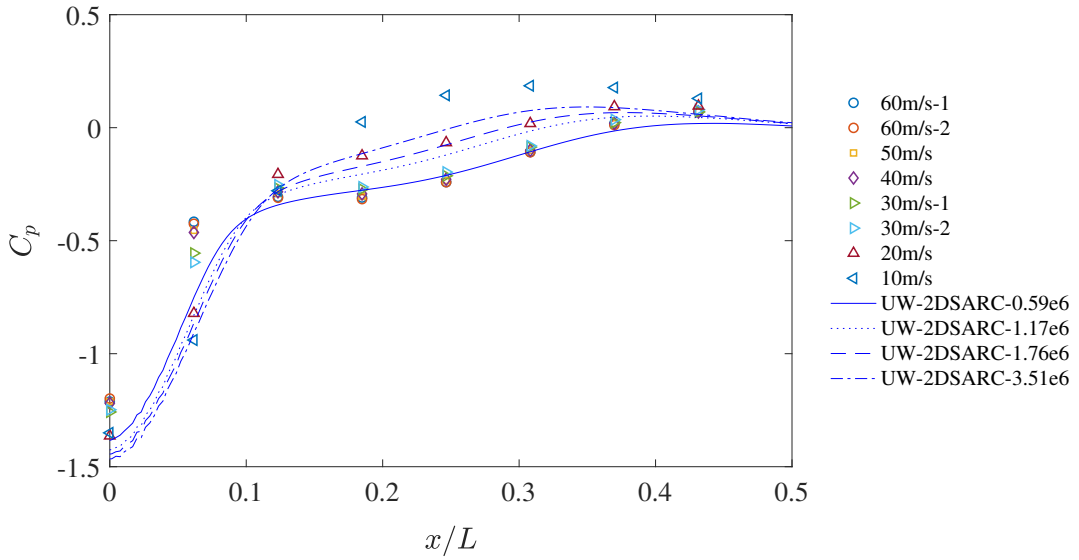

Figure 4.13: Variation in pressure along the streamwise centerline, highlighting the separated region.

believed to be more indicative of what is occurring in the flow. According to the flow visualization, the geometry of the separated region is changing with velocity. However, the flow visualization method chosen is prone to bias due to the pool of china clay liquid which would form in the separated region and the sputtering of droplets onto the bump. The surface static pressure measurements were conducted in a more robust way than the flow visualization was capable. The surface pressure data give a more refined picture of the flow, while the flow visualization gives a more qualitative picture.

When looking at the surface static pressure data along the centerline, the disagreement between the 2D-SARC simulations and the experimental data in the separated region (Figure 4.13) should be noted and are worth further discussion. For $x/L < 0.1$, the experimental data show a trend of lower pressures with lower Reynolds numbers. In the $0.1 < x/L < 0.45$ region, experimental data show higher pressures for lower Reynolds numbers. The simulation data show the opposite in both regions–lower pressures for higher Reynolds for $x/L < 0.1$ and lower higher pressures at lower Reynolds numbers for $0.1 < x/L < 0.45$. This suggests the 2D

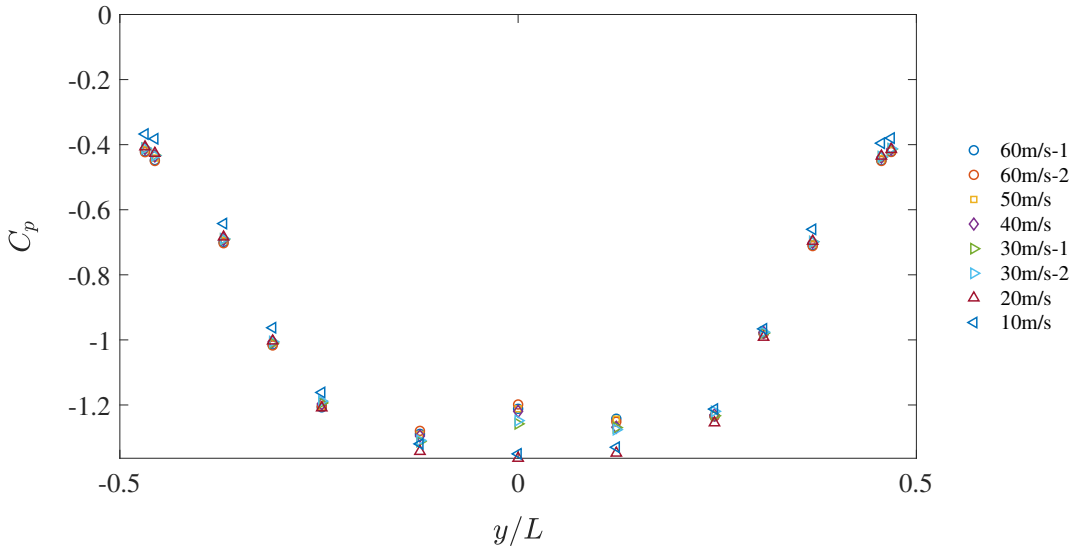

Figure 4.14: Variation in pressure along the ridge of the bump ($x = 0$). Cases as in Figure 4.12.

SARC is significantly challenged by this flow geometry. Given the point of this project is to push CFD to some of its current limits, having a flow geometry where the model clearly does not agree with the experiment is desirable and evident of a well designed experiment for the purposes of CFD improvement.

Chapter 5

CONCLUSION

A splitter plate and a speed bump geometry were designed and constructed to examine turbulent flow separation. The bump geometry is Gaussian in the streamwise direction and an error function in the spanwise in an effort to minimize side wall effects. The splitter plate allowed the placement of the leading edge stagnation point by adjusting the angle of a trailing edge flap via a turnbuckle. Qualification of the wind tunnel found the flow freestream turbulence and mean uniformity to be suitable for this validation test.

A range of tripping devices were examined to determine their effect on the boundary layer upstream of the bump. The boundary layer was found to be turbulent for all tripping devices for 30 and 60m/s freestream velocities. Since all tripped boundary layers showed nearly identical characteristics, the smallest trip, the 240-grit sandpaper, was chosen to be used for all further studies. The wake component of the mean velocity profile, as compared with Coles' correlation for fully turbulent and optimally-tripped boundary layers [4], was also acceptable.

The separated flow over the bump geometry was studied for $0.69 < Re_L < 3.60(\times 10^6)$, using a combination of china clay flow visualization and 48 surface pressure taps. The flow visualization showed macro scale features of the flow, such as the clear presence of a separation bubble. The surface pressure data suggest invariance of the pressures in the separated region at high Reynolds number (above 30 m/s) on both the plate and bump. The pressures measured along the spanwise ridge of the bump show three-dimensionality present all the way to the centerline of the bump. A comparison of experimental and 2D RANS simulation show the simulation data are close to the experimental data in magnitude. However, experimental and simulated surface pressure data indicate opposite Reynolds number trends in

the separated region.

Overall, this thesis represents a successful beginning to a larger project aiming to provide a test case for validating current and future turbulence models and simulations. Key flow parameters of the test geometry were qualified. A correctly tripped boundary layer is known to develop with the current set-up. An initial investigation of the separated region indicates a flow which 2D RANS currently struggles to model accurately, showing a test worth using to validate CFD models of turbulent separated flows.

An immediate continuation of this project will examine boundary layer data corresponding to the lowest tunnel velocities for which surface pressure data was acquired in order to help determine the trip effectiveness at these lower Reynolds numbers. Flow field measurements using particle image velocimetry (PIV) are also planned, producing flowfield turbulent kinetic energy data central to many current models, and helping determine the source of discrepancies between simulations and the current test case.

Appendix A

PRESSURE TAP POSITIONS ON BUMP SURFACE

Table A.1: Summary of pressure tap locations and measured C_p for U = 30 and 60m/s. Table organized by spanwise plane number indicated in Figure 3.5a.

Tap No.	**Plane**	y/L_b	x/L_b	y/L	x/L	C_p Re_L = 3.6e6, 60 – 2	C_p Re_L = 1.8e6, 30 – 2
0	0	0.0000	-0.9261	0.0000	-0.9132	-	-
1		0.0000	-0.8415	0.0000	-0.8299	5.36e – 03	4.32e – 04
2		0.0000	-0.7570	0.0000	-0.7465	6.82e – 03	1.08e – 03
3		0.0000	-0.3750	0.0000	-0.3698	1.99e – 01	1.86e – 01
4		0.0000	-0.2500	0.0000	-0.2465	2.29e – 01	2.13e – 01
5		0.0000	-0.1250	0.0000	-0.1233	−2.50e – 01	−2.61e – 01
6		0.0000	-0.0625	0.0000	-0.0616	−9.07e – 01	−9.19e – 01
7		0.0000	0.0000	0.0000	0.0000	−1.20e + 00	−1.26e + 00
8		0.0000	0.0625	0.0000	0.0616	−4.25e – 01	−5.55e – 01
9		0.0000	0.1250	0.0000	0.1233	−3.10e – 01	−2.68e – 01
10		0.0000	0.1875	0.0000	0.1849	−3.16e – 01	−2.72e – 01
11		0.0000	0.2500	0.0000	0.2465	−2.41e – 01	−2.13e – 01
12		0.0000	0.3125	0.0000	0.3082	−1.09e – 01	−8.59e – 02
13		0.0000	0.3750	0.0000	0.3698	1.16e – 02	2.23e – 02
14		0.0000	0.4375	0.0000	0.4314	7.28e – 02	6.97e – 02
15		0.0000	0.5704	0.0000	0.5625	4.93e – 02	3.93e – 02
16		0.0000	0.6831	0.0000	0.6736	8.08e – 03	−1.93e – 03
17		0.0000	0.7958	0.0000	0.7847	−1.05e – 02	−2.05e – 02
18		0.0000	0.9085	0.0000	0.8958	−2.28e – 02	−3.05e – 02
19		0.0000	1.0211	0.0000	1.0069	−4.19e – 02	−4.69e – 02
20		0.0000	1.1338	0.0000	1.1181	−1.25e + 00	−1.27e + 00
21	1	0.1250	0.0000	0.1233	0.0000	−1.28e + 00	−1.31e + 00
22		-0.1250	0.0000	-0.1233	0.0000	−3.45e – 01	−3.08e – 01
23		0.1250	0.1250	0.1233	0.1233	−3.47e – 01	−3.07e – 01
24		-0.1250	0.1250	-0.1233	0.1233	−2.21e – 01	−1.89e – 01
25		0.1250	0.2500	0.1233	0.2465	−1.55e – 01	−1.08e – 01
26		-0.1250	0.2500	-0.1233	0.2465	−4.44e – 02	−6.02e – 02

Continued on next page

Table A.1 – continued from previous page

Tap No.	**Plane**	y/L_b	x/L_b	y/L	x/L	C_p Re_L = 3.6e6, 60 – 2	C_p Re_L = 1.8e6, 30 – 2
27		0.1250	0.3125	0.1233	0.3082	1.68e – 02	−1.36e – 02
28		-0.1250	0.3125	-0.1233	0.3082	7.98e – 02	6.18e – 02
29		0.1250	0.3750	0.1233	0.3698	1.42e – 01	1.45e – 01
30		-0.1250	0.3750	-0.1233	0.3698	1.73e – 01	1.64e – 01
31	2	0.2500	-0.3750	0.2465	-0.3698	1.70e – 01	1.61e – 01
32		-0.2500	-0.3750	-0.2465	-0.3698	−1.23e + 00	−1.23e + 00
33		0.2500	0.0000	0.2465	0.0000	−1.20e + 00	−1.19e + 00
34		-0.2500	0.0000	-0.2465	0.0000	−1.60e – 01	−1.65e – 01
35		0.2500	0.1875	0.2465	0.1849	−1.52e – 01	−1.37e – 01
36		-0.2500	0.1875	-0.2465	0.1849	−9.80e – 01	−9.79e – 01
37	3	0.3125	0.0000	0.3082	0.0000	−1.02e + 00	−1.01e + 00
38		-0.3125	0.0000	-0.3082	0.0000	−7.12e – 01	−6.98e – 01
39	4	0.3750	0.0000	0.3698	0.0000	−7.03e – 01	−6.90e – 01
40		-0.3750	0.0000	-0.3698	0.0000	−6.42e – 02	−6.88e – 02
41	5	0.4625	-0.2500	0.4561	-0.2465	−6.88e – 02	−7.17e – 02
42		-0.4625	-0.2500	-0.4561	-0.2465	−4.50e – 01	−4.38e – 01
43		0.4625	0.0000	0.4561	0.0000	−4.50e – 01	−4.33e – 01
44		-0.4625	0.0000	-0.4561	0.0000	−1.21e – 01	−1.21e – 01
45		0.4625	0.2500	0.4561	0.2465	−1.23e – 01	−1.27e – 01
46		-0.4625	0.2500	-0.4561	0.2465	−4.22e – 01	−4.14e – 01
47	6	0.4750	0.0000	0.4684	0.0000	−4.23e – 01	−4.11e – 01
48		-0.4750	0.0000	-0.4684	0.0000	−2.99e – 02	−3.36e – 02

BIBLIOGRAPHY

[1] Lee, T. and Mateescu, D., "Experimental and Numerical Investigation of 2-D Backward-Facing Step Flow," *Journal of Fluids and Structures*, Vol. 12, No. 6, 1998, pp. 703 – 716.

[2] Byun, G., *Sturcture of Three-Dimensional Separated Flow on Symmetric Bumps*, Ph.D. thesis, Virginia Tech, 2005.

[3] McKeon, B., Li, J., W., J., Morrison, J., and Smits, A., "Pitot probe corrections in fully developed turbulent pipe flow," *Measurement Science and Technology*, Vol. 14, 2003, pp. 1449–1458.

[4] Coles, D., "The turbulent boundary layer in a compressible fluid," Tech. rep., Report R-403-PR, The Rand Corporation, Santa Monica, California, 1962.

[5] Samuell, M., "Simulation Study of 2D Separated Turbulent Flows," Unpublished.

[6] Slotnick, J., Khodadoust, A., Alonso, J., Darmofal, D., Gropp, W., Lurie, E., and Mavriplis, D., "CFD Vision 2030 Study: A Path to Revolutionary Computational Aerosciences," Tech. rep., NASA, 2014.

[7] Oberkampf, W. L. and Smith, B., *Assessment Criteria for Computational Fluid Dynamics Validation Benchmark Experiments*.

[8] Greenblatt, D., Paschal, K., Schaeffler, N., Washburn, A., and Yao, C., "Separation Control over a Wall-Mounted Hump: A CFD Validation Test Case," *Proceedings of the 2004 Workshop on CFD Validation of Synthetic Jets and Turbulent Separation Control*, NASA, 4 2007.

[9] Bell, J., Heineck, J., Zilliac, G., Mehta, R., and Long, K., "Surface and Flow Field Measurements on the FAITH Hill Model," *50th AIAA Aerospace Sciences Meeting including the New Horizons Forum and Aerospace Exposition*.

[10] Driver, D., "Reynolds shear stress measurements in a separated boundary layer flow," *22nd Fluid Dynamics, Plasma Dynamics and Lasers Conference*.

[11] Bachalo, W. D. and Johnson, D. A., "Transonic, turbulent boundary-layer separation generated on an axisymmetric flow model," *AIAA Journal*, Vol. 24, No. 3, 1986, pp. 437–443.

[12] Araujo, P. P. and Rezende, A. L. T., "Comparison of Turbulence Models in the Flow over a Backward-Facing Step," *International Journal of Engineering Research & Science*, Vol. 3, No. 11, 2017, pp. 88–93.

[13] Armaly, B. F., Durst, F., Pereira, J. C. F., and Schönung, B., "Experimental and theoretical investigation of backward-facing step flow," *Journal of Fluid Mechanics*, Vol. 127, 1983, pp. 473–496.

[14] Durst, F. and Tropea, C., "Flows over Two-Dimensional Backward-Facing Steps," *Structure of Complex Turbulent Shear Flow*, edited by R. Dumas and L. Fulachier, Springer, Berlin, Heidelberg, 1983, pp. 41–52.

[15] Nakagawa, H. and Nezu, I., "Experimental investigation on turbulent structure of backward-facing step flow in an open channel," *Journal of Hydraulic Research*, Vol. 25, No. 1, 1987, pp. 67–88.

[16] Thangam, S. and Knight, D. D., "Effect of stepheight on the separated flow past a backward facing step," *Physics of Fluids A: Fluid Dynamics*, Vol. 1, No. 3, 1989, pp. 604–606.

[17] Kostas, J., Soria, J., and Chong, M., "Particle image velocimetry measurements of a backward-facing step flow," *Experiments in fluids*, Vol. 33, No. 6, 2002, pp. 838–853.

[18] Byun, G. and Simpson, R. L., "Structure of three-dimensional separated flow on an axisymmetric bump," *AIAA journal*, Vol. 44, No. 5, 2006, pp. 999–1008.

[19] Ishihara, T., Hibi, K., and Oikawa, S., "A wind tunnel study of turbulent flow over a three-dimensional steep hill," *Journal of Wind Engineering and Industrial Aerodynamics*, Vol. 83, No. 1-3, 1999, pp. 95–107.

[20] Simpson, R. L., Long, C., and Byun, G., "Study of vortical separation from an axisymmetric hill," *International Journal of Heat and Fluid Flow*, Vol. 23, No. 5, 2002, pp. 582–591.

[21] Simmons, D. J., Thomas, F. O., and Corke, T. C., "Benchmark Smooth Body Flow Separation Experiments," *47th AIAA Fluid Dynamics Conference*, 2017, p. 4128.

[22] Ma, R. and Simpson, R. L., "Characterization of turbulent flow downstream of a three-dimensional axisymmetric bump," *4th International Symposium on Turbulence and Shear Flow Phenomena*, Begel House Inc., 2005.

[23] Patel, N. and Menon, S., "Structure of flow separation and reattachment behind an axisymmetric hill," *Journal of Turbulence*, , No. 8, 2007, pp. N36.

[24] Byun, G., Simpson, R. L., and Long, C., "Study of vortical separation from three-dimensional symmetric bumps," *AIAA journal*, Vol. 42, No. 4, 2004, pp. 754–765.

[25] Byun, G. and Simpson, R. L., "Surface-pressure fluctuations from separated flow over an axisymmetric bump," *AIAA journal*, Vol. 48, No. 10, 2010, pp. 2397–2405.

[26] Garcia-Villalba, M., Li, N., Rodi, W., and Leschziner, M., "Large-eddy simulation of separated flow over a three-dimensional axisymmetric hill," *Journal of fluid Mechanics*, Vol. 627, 2009, pp. 55–96.

[27] Long, C., *A study of vortical separation from symmetric bumps*, Master's thesis, Virginia Polytechnic Institute and State University, 2002.

[28] Patel, N., Stone, C., and Menon, S., "Large-eddy simulation of turbulent flow over an axisymmetric hill," *41st Aerospace Sciences Meeting and Exhibit*, 2003, p. 967.

[29] Wang, C., Jang, Y., and Leschziner, M., "Modelling two-and three-dimensional separation from curved surfaces with anisotropy-resolving turbulence closures," *International Journal of Heat and Fluid Flow*, Vol. 25, No. 3, 2004, pp. 499–512.

[30] Jørgensen, F. E., *How to measure turbulence with hot-wire anemometers - a practical guide*, Dantec Dynamics, P.O. Box 121, Tonsbakken 16-18, DK-2740 Skovlunde, Denmark, 1st ed., 02 2002.

[31] Hultmark, M. and Smits, A. J., "Temperature corrections for constant temperature and constant current hot-wire anemometers," *Measurement Science and Technology*, Vol. 21, No. 10, Aug 2010, pp. 105404.

[32] Hanson, R. E., Buckley, H. P., and Lavoie, P., "Aerodynamic optimization of the flat-plate leading edge for experimental studies of laminar and transitional boundary layers," *Experiments in fluids*, Vol. 53, No. 4, 2012, pp. 863–871.

[33] Clauser, F. H., "Turbulent boundary layers in adverse pressure gradients," *Journal of Aerospace Sciences*, Vol. 21, 1954, pp. 91–108.

[34] Shur, M. L., Strelets, M. K., Travin, A. K., and Spalart, P. R., "Turbulence Modeling in Rotating and Curved Channels: Assessing the Spalart-Shur Correction," *AIAA Journal*, Vol. 38, No. 5, 2000, pp. 784–792.

[35] Schlichting, H., *Boundary Layer Theory*, McGraw-Hill, 1979.